

Supplementary Information for:

A Carbon Nanotube Reporter of miRNA Hybridization Events In Vivo

Jackson D. Harvey^{1,2}, Prakrit V. Jena¹, Hanan A. Baker^{1,2}, Gül H. Zerze³, Ryan M. Williams¹,
Thomas V. Galassi^{1,2}, Daniel Roxbury⁴, Jeetain Mittal³, Daniel A. Heller^{1,2*}

¹Memorial Sloan Kettering Cancer Center, New York, NY

²Weill Cornell Medical College, New York, NY

³Lehigh University, Bethlehem, PA

⁴University of Rhode Island, Kingston, RI

Table of contents

Supplementary Text

Thermodynamic analysis of nucleic acid hybridization on the sensor.....	6
Effects of amphipathic molecules on sensor response	6
SDBS-induced spectroscopic changes.....	8
Molecular weight of the sensor complex.....	9

Supplementary Figures

Figure S1. Selectivity assessment of different nanotube binding domains.....	11
Figure S2. Photoluminescence excitation/emission plots of the GT15mir19 sensor.....	12
Figure S3. Intensity response of the GT15mir19 sensor.....	12
Figure S4. Plots of excitation and emission wavelength shifts.....	13
Figure S5. Atomic force microscopy of the GT15mir19 complex under dry conditions.....	14
Figure S6. Atomic force microscopy of the GT15mir19 complex under aqueous conditions....	15
Figure S7. Cartoon depicting the fluorophore dequenching of GT6mir19-Cy5 upon binding of the target miR-19 DNA sequence.....	16
Figure S8. Near-infrared emission wavelength response of the modified sensor complex, GT6mir19-Cy5, used for the fluorophore dequenching experiment.....	16
Figure S9. Structural parameters of the GT15mir19 sensor complex computed for the (9,4) nanotube via molecular dynamics simulations.....	17
Figure S10. Starting configurations of molecular dynamics simulations involving the duplex miRNA capture sequence + miR-19 without the GT ₁₅ nanotube binding domain.....	18
Figure S11. Two calculations of hybridization free energy of DNA on the nanotube surface.....	19

Figure S12: Mean peak wavelength and intensity values of the GT15mir19 complex after incubation with amphipathic molecules.....	20
Figure S13: Change of the GT15mir19 sensor response to miRNA upon interrogation with a panel of amphiphilic molecules.....	20
Figure S14. Photoluminescence excitation/emission plots of the GT15mir19 sensor with 0.2% SDBS.....	21
Figure S15. Excitation and emission wavelength shifts of the GT15mir19 sensor, calculated from photoluminescence excitation/emission (PL) plots.....	22
Figure S16. Change in intensity of the GT15mir19 sensor in the presence of 0.2% SDBS.....	23
Figure S17. Diameter dependence of emission energy change and intensity change.....	24
Figure S18. Emission response of the GT15mir19 sensor to different SDBS concentrations, in the absence of analyte.....	25
Figure S19. Wavelength response of the GT15mir19 sensor in the presence of random permutations of DNA 23 nucleotides in length.....	26
Figure S20: Emission wavelength response of GT15mirX sensors.....	27
Figure S21: Intensity response of the GT15mirX sensors after the introduction of target miR sequences or R23 non-complementary control.....	28
Figure S22. Kinetic response of the GT15mirX sensor to three closely-related sequences.....	28
Figure S23. Kinetic response of the GT15mirX sensor to three closely-related sequences.....	29
Figure S24. Dose-response curves of the GT15mir19 sensor response, using three different sensor concentrations.....	29
Figure S25. Kinetic data for all measured chiralities of the GT15mir19 sensor.....	30

Figure S26. Comparison of the response rate of the GT15mir19 sensor to DNA or RNA versions of the target, for eleven different nanotube chiralities.....	31
Figure S27. Kinetics of the wavelength response of GT15mirX sensors after addition of target miR biomarker sequences.....	32
Figure S28. GT15mirX sensor response rates vs. guanine content of the miRNA capture sequences.....	32
Figure S29. GT15mirX sensor response rates vs. thymine, adenosine, and cytosine content of the miRNA capture sequence, or free energy of hybridization of the miRNA capture sequence.....	33
Figure S30. GT15mirX sensor response rates vs. thymine, adenosine, and cytosine content of the miRNA capture sequence, or free energy of hybridization of the miRNA capture sequence.....	34
Figure S31. Single-GT15mir19 spectra measured via near-infrared hyperspectral microscopy.....	35
Figure S32. Normalized absorbance spectra of GT15mir19 oligonucleotide-suspended APT-200 from Nano-C and GT15mir509 oligonucleotide-suspended CoMoCAT.....	36
Figure S33. Sensor response in urine from healthy donors.....	37
Figure S34. Study of the sensor response in serum.....	38
Figure S35: Intensity response of the GT15mir21 sensor after introducing the miR-21 RNA oligonucleotide in serum with proteinase K.....	38
Figure S36. Persistence of wavelength shifting of the GT15mir19 sensor upon dialysis of SDBS	39
Figure S37: Response of the implanted sensor device to 1 nanomole of miR-19 RNA	

within live mice.....	39
Figure S38. Dose-response curve of the GT15mir19 sensor capillary device measured in vitro.....	40
Figure S39: Emission from the implantable devices removed from one animal in each group...	40
Supplementary Tables	
Table S1: List of amphipathic molecules used to study the enhancement of the sensor response.....	41
Table S2. GT15mirX sequences used in this work.....	41
Table S3. Analyte/target sequences used in this work.....	42
Table S4. Truncated miR analyte sequences designed to hybridize to the middle of miRNA capture sequence.....	42
Table S5. Truncated miR analyte sequences designed to hybridize to the 5' end of miRNA capture sequence.....	43
Table S6. Elongated analyte sequences used in this work.....	43
References.....	43

Supplementary Text

Thermodynamic analysis of nucleic acid hybridization on the sensor

We used the two schemes shown in Figure S11 to estimate the difference in free energy of ssDNA adsorption and dsDNA hybridization at the nanotube surface. As parameters needed for such a calculation are available from Jung et al.¹ for a 17-mer duplex strand, we focus our analysis for this particular DNA length and sequence. For case A, one ssDNA is already adsorbed on the nanotube surface and its complementary partner ssDNA is introduced in the solution like the experimental setup reported in this paper. The change in free energy upon hybridization is approximately -135 kcal/mol (at (300 K, 1 bar), which clearly indicates that hybridization is preferred over adsorption. Similar analysis for case B, where both strands are initially adsorbed on the nanotube surface, the change in free energy upon hybridization (again using values reported by Jung et al.) is approximately +9 kcal/mol. This indicates that when both strands are initially adsorbed (Figure S11 Case B), ssDNA adsorption is slightly more favorable than dsDNA hybridization. In our experimental setup of miR-19 hybridization on the nanotube, we expect the case A to be the relevant one as complementary strand is introduced after ssDNA and surfactant are allowed to adsorb on the nanotube surface. Thus, our analysis findings are consistent with the observed hybridization leading to the function of biosensor / reporter.

Effects of amphipathic molecules on sensor response

Several classes of amphipathic molecules were introduced to the GT15mir19 sensor to assess their potential to modulate the optical response to hybridization. Selected molecules included ionic surfactants, non-ionic triblock copolymers, non-ionic surfactants, PEG-functionalized lipid, and BSA due to their variety of steric and electrostatic properties (Table S1). After treatment for 4 hours with each amphipathic molecule, but before addition of target oligonucleotide, emission

spectra were measured to assess the effect of each molecule in the absence of target miRNA. The impact on center wavelength and intensity are shown for the (7,5) nanotube, which was similar to the responses of other chiralities (Figure S12). All molecules either elicited a blue-shift to varying degrees or had no apparent effect. SDC was an outlier in that the intensity was enhanced 2-3 fold. While other molecules were found to also enhance intensity to different degrees, none matched the effect of SDC.

For each set of surfactant-treated nanotubes, complementary and non-complementary target oligonucleotides were introduced and incubated for 4 hours. Each amphipathic molecule was tested at a final concentration of 0.2% wt/vol with 2 mg/L of GT15mir19. Endpoint data showed that SDBS and IGEPAL provided the greatest enhancement of target miRNA-induced blue-shifting, followed by SDS, Brij52, and lipid-PEG to a smaller extent (Figure S13). The presence of Pluronic, SDC, and Triton X-100 resulted in no apparent blue-shift of the sensor upon introduction of target miRNA, although we note that SDC and Triton X-100 substantially blue-shifted the nanotube before target oligonucleotides were added. The initial blue-shift suggests that these amphiphiles likely coated the nanotube so efficiently as to displace water from the nanotube surface and prevent the capture sequence of the GT15mir19 oligonucleotide from interacting with the nanotube surface prior to hybridization. There are no obvious patterns relating the structure of the amphiphiles to the modulation of the response to miRNA, although there are certain factors that can be noted. It is not surprising that SDC caused an initial blue-shift and prevented the response to miRNA, for example, because it is a very strong surfactant that is known to efficiently suspend nanotubes and enhance nanotube emission. Pluronic and Triton X-100 are fairly large/bulky surfactant molecules which may have similarly prevented

interactions of the capture sequence with the nanotube surface. We also note the structural similarity between SDBS and IGEPAL, the two surfactants that resulted in the largest hybridization-induced enhancements. The supramolecular interactions of the surfactant molecules with each other and the nanotube surface are complex and warrant further study in this context.

SDBS-induced spectroscopic changes

Previous work has shown that the optical transition energies for DNA-wrapped nanotubes are red-shifted by 10-20 meV (14-22 nm, depending on chirality) and quenched as compared to nanotubes suspended entirely with small molecule anionic surfactants like SDS or SDBS²⁻⁴. A proposed mechanism has attributed this finding to incomplete coverage of the nanotube surface by DNA, which allows for greater accessibility of water, resulting in an increased polarity of the local solvent environment (higher local dielectric constant) in the immediate vicinity of the nanotube⁴. In the current work, we observed a blue-shifted shoulder in the spectrum of the GTmir19 sensor in the absence of the complementary miR-19 strand upon introduction of SDBS (Figure 1h and S14). In light of previous findings, this spectral change suggests that SDBS binds to the exposed surfaces on the DNA-suspended nanotube, causing the displacement of water from the nanotube surface, which produces a slight blue-shift in the emission. When target RNA or DNA hybridizes and the duplex dissociates from the surface, bare nanotube surface is exposed, allowing SDBS to bind and become the dominant factor determining of the nanotube emission peak wavelength, and intensity. The net effect was a dramatic blue-shift (4-17 nm, depending on the nanotube chirality) and intensity increase (1.3 -2.2 fold) from the assembly of supramolecular complexes of SDBS, triggered by the introduction of target RNA or DNA.

From spectroscopic studies of the GT15mir19 sensor response, we observed a blue shift in nanotube excitation wavelengths, suggesting that the binding of miR-19 RNA and DNA affects the ground state absorption energies in addition to the excited state. Figure S15a shows the correlation between the excitation wavelength shift and the emission wavelength shift for the ensemble of chiralities, yielding a Pearson correlation coefficient of 0.87744 ($p=0.00188$). When plotted as change in energy (Figure S15b), the Pearson correlation coefficient is similar 0.90656 ($p=0.0007$). The environmental effects on nanotube optical properties have been shown to depend at least in part on the mod type of the nanotube⁵. On stratifying the nanotubes by mod type, defined for any nanotube as $\text{mod}(n-m,3)$, we found that mod2 nanotubes exhibited an emission energy modulation that increased nearly linearly ($R^2=0.9272$) with nanotube diameter (Figure S16a). Interestingly, for the mod2 nanotubes, the intensity enhancement did not show the same linear relationship with nanotube diameter, although all nanotubes increased in intensity. A maximum was found for nanotubes ~ 0.9 nm in diameter (Figure S16b). A slight difference also became apparent between the responses to target DNA and RNA, with RNA eliciting a slightly enhanced intensity increase for small diameter nanotubes and a slightly dampened enhancement for larger diameter nanotubes. This small, diameter-dependent difference may be related to the difference in binding strength and hydration between DNA-DNA hybrids and DNA-RNA hybrids^{6,7}.

Molecular weight of the sensor complex

The molecular weight of the sensor was estimated using the lower limit of the nanotube diameters to be 0.8 nm, wherein there are 20 carbons around the nanotube circumference. Thus, 80 carbon atoms are present for every 0.283 nm in nanotube length. Taking the average length of

the nanotube, as measured via AFM, to be 166 nm, the resulting molecular weight of the nanotube is 564 kDa. The molecular weight of the GT15mir19 DNA sequence is 16.5 kDa. From AFM measurements, we estimated 5-10 copies of DNA per 100 nm, and thus 8.3 to 16.6 copies per 166 nm, adding 137 kDa to 275 kDa to the total complex. Thus, for an average length GT15mir19 sensor with diameter near the lower limit, the molecular weight would be between 701 kDa and 839 kDa.

Supplementary Figures

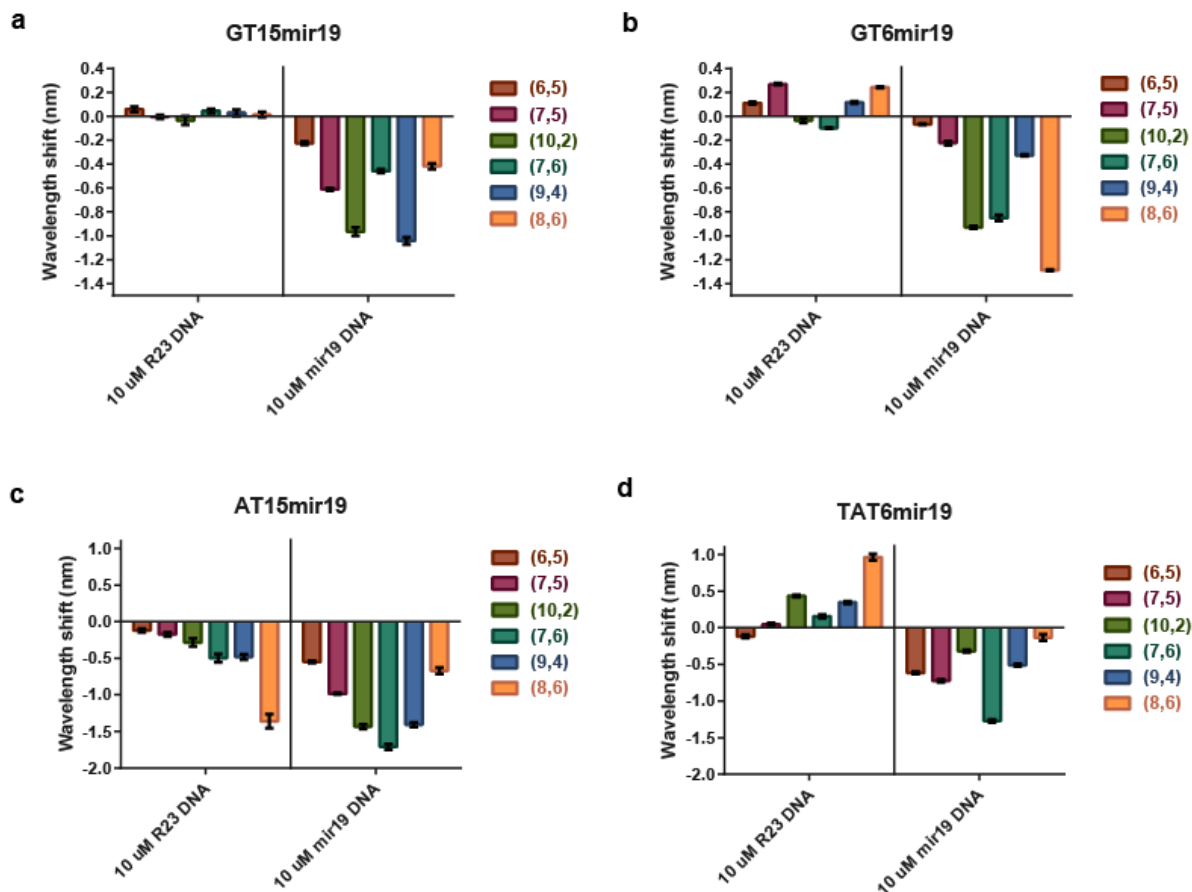


Figure S1. Selectivity assessment of different nanotube binding domains. Wavelength shift of modified sensors after addition of non-complementary control (R23) or miR-19 DNA. **a**, Sensor composed of the (GT)₁₅ nanotube binding sequence (GT15mir19). **b**, Sensor composed of the (GT)₆ nanotube binding sequence (GT6mir19). **c**, Sensor composed of the (AT)₁₅ nanotube binding sequence (AT15mir19). **d**, Sensor composed of the (TAT)₆ nanotube binding sequence (TAT6mir19). Error bars represent standard deviation for n = 3 technical replicates.

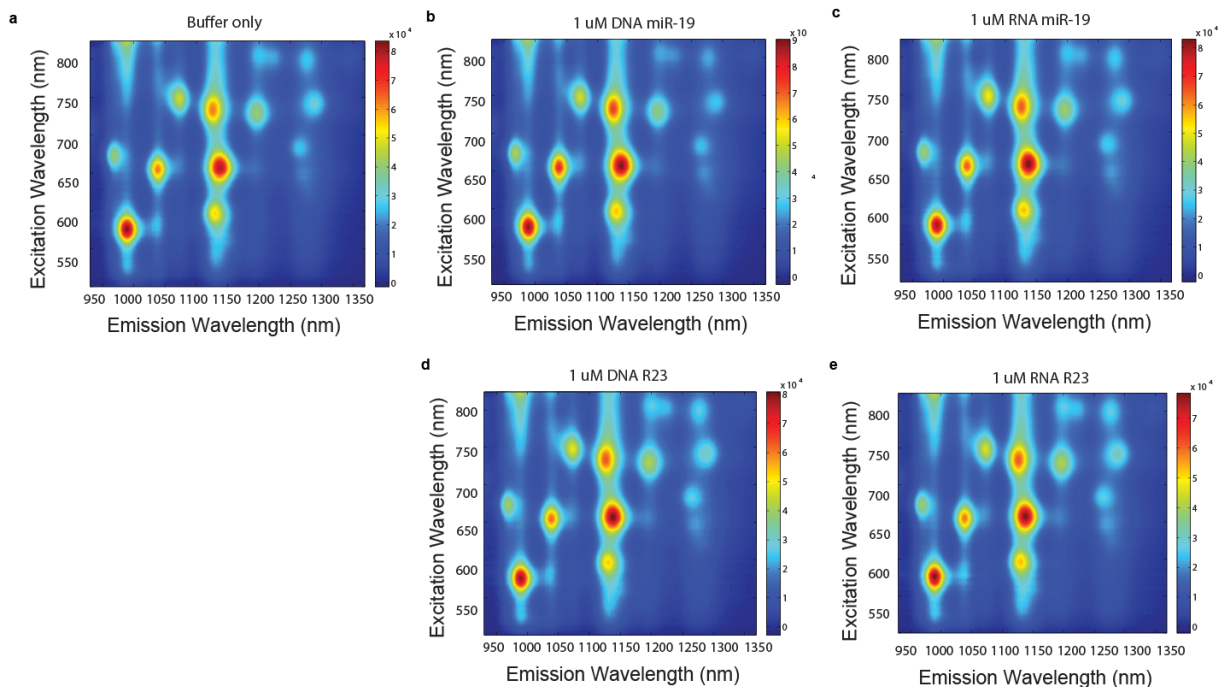


Figure S2. Photoluminescence excitation/emission plots of the GT15mir19 sensor **a**, in buffer only, **b**, after interrogation with miR-19 DNA, **c**, after interrogation with miR-19 RNA, **d**, after interrogation with R23 DNA, **e**, after interrogation with R23 RNA.

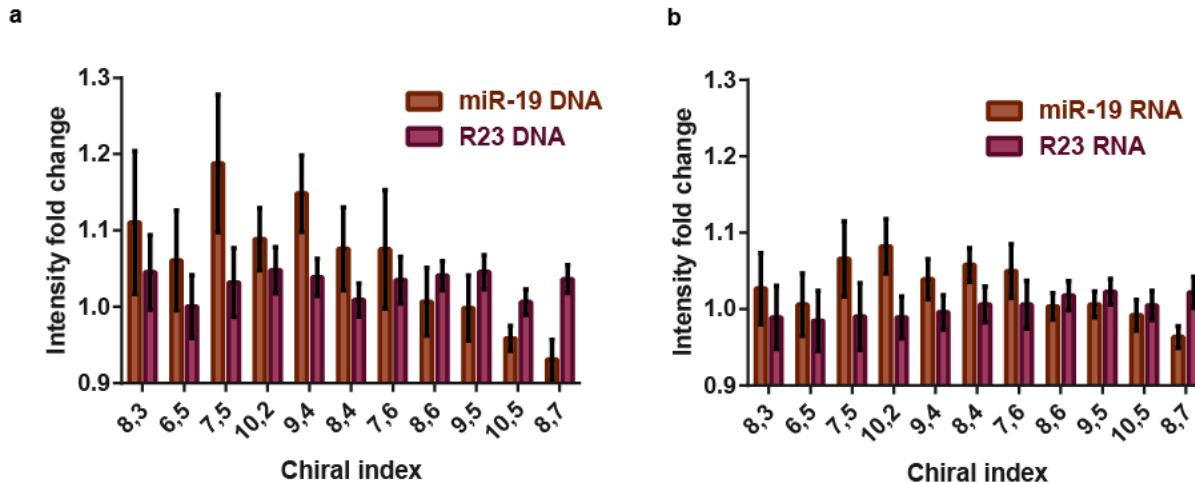


Figure S3. Intensity response of the GT15mir19 sensor. **a**, Response after addition of miR-19 DNA analogue or random sequence DNA control. **b**, Response after addition of miR-19 RNA or random sequence RNA control. Error bars represent standard deviation for $n = 3$ technical replicates.

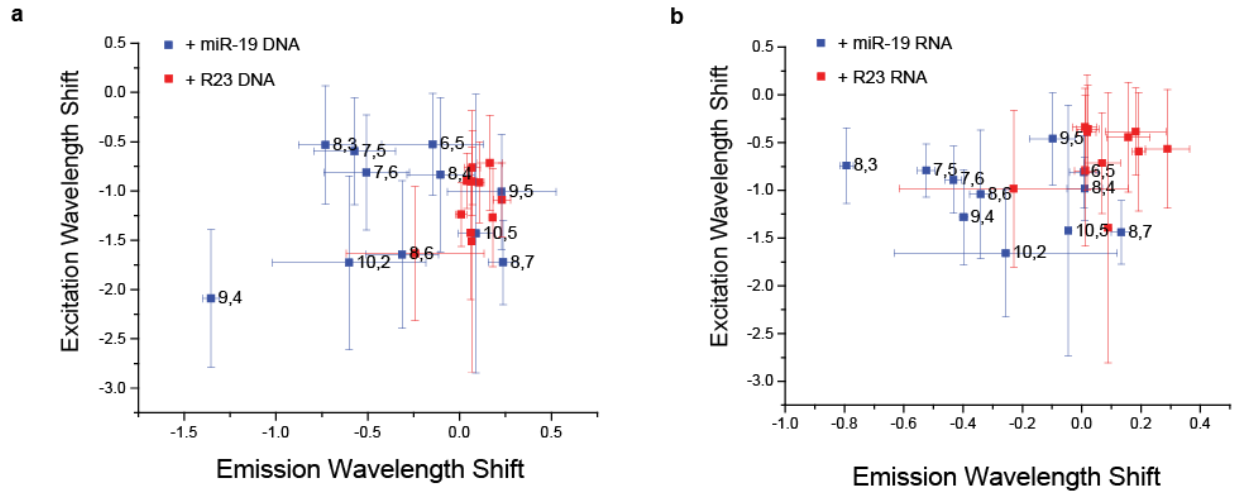


Figure S4. Plots of excitation and emission wavelength shifts calculated from photoluminescence plots. **a**, Responses to miR-19 DNA analogue and random sequence DNA control (R23). **b**, Responses to miR-19 RNA and random sequence RNA control (R23). Error bars represent standard deviation for $n = 3$ technical replicates.

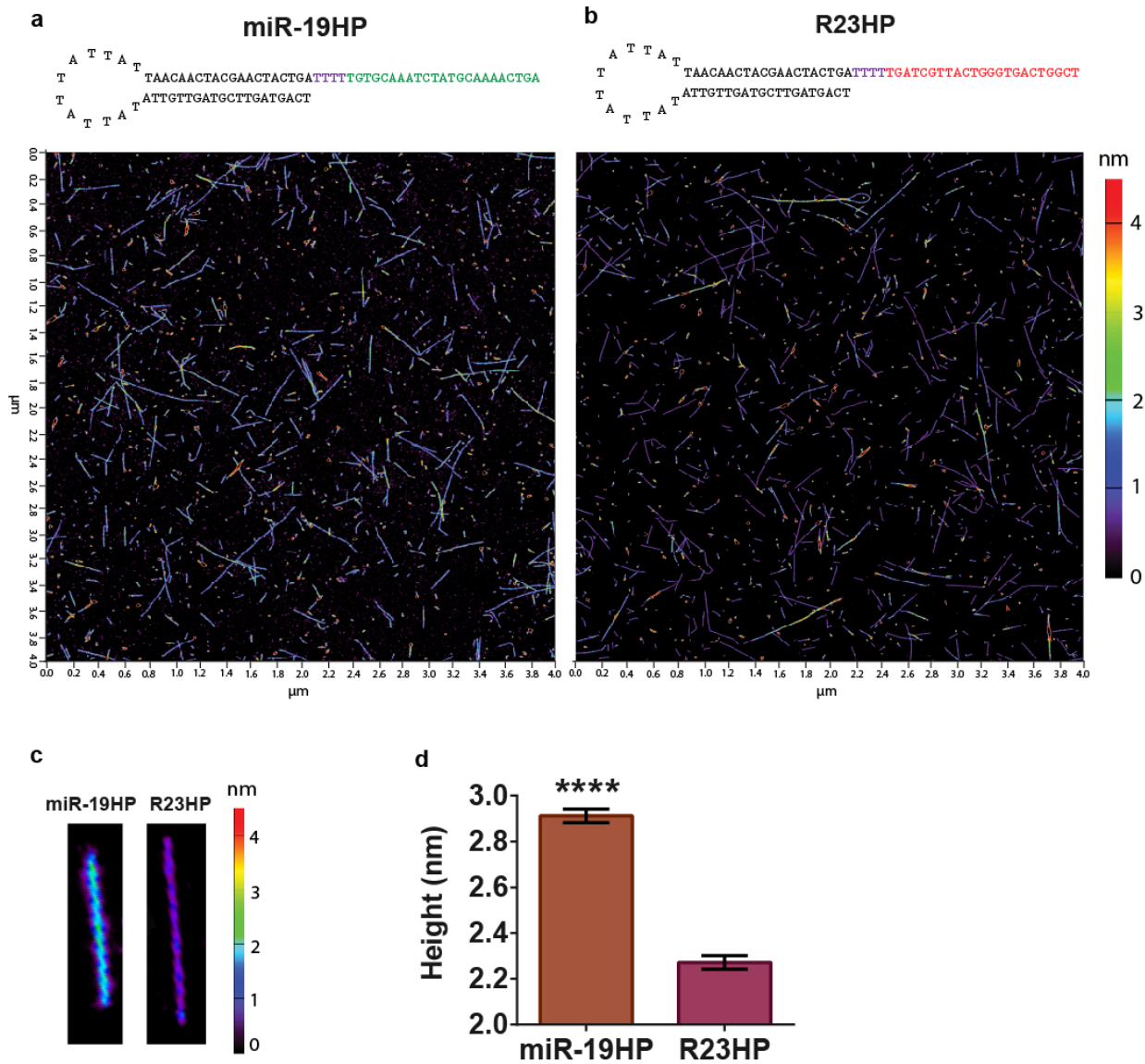


Figure S5. Atomic force microscopy of the GT15mir19 complex under dry conditions. **a** and **b**, Sequences of the hairpin RNAs miR-19HP and R23HP, respectively, and AFM height profiles after incubation. Green bases are complementary to the GT15mir19 capture sequence, red bases are random sequence control, and purple bases are thymine spacers. **c**, Images of single nanotubes from miR-19HP and R23HP images. **d**, Average height of nanotubes after addition of miR-19HP or R23HP, calculated from $n = 1332$ nanotubes. Error bars represent standard error of the mean.

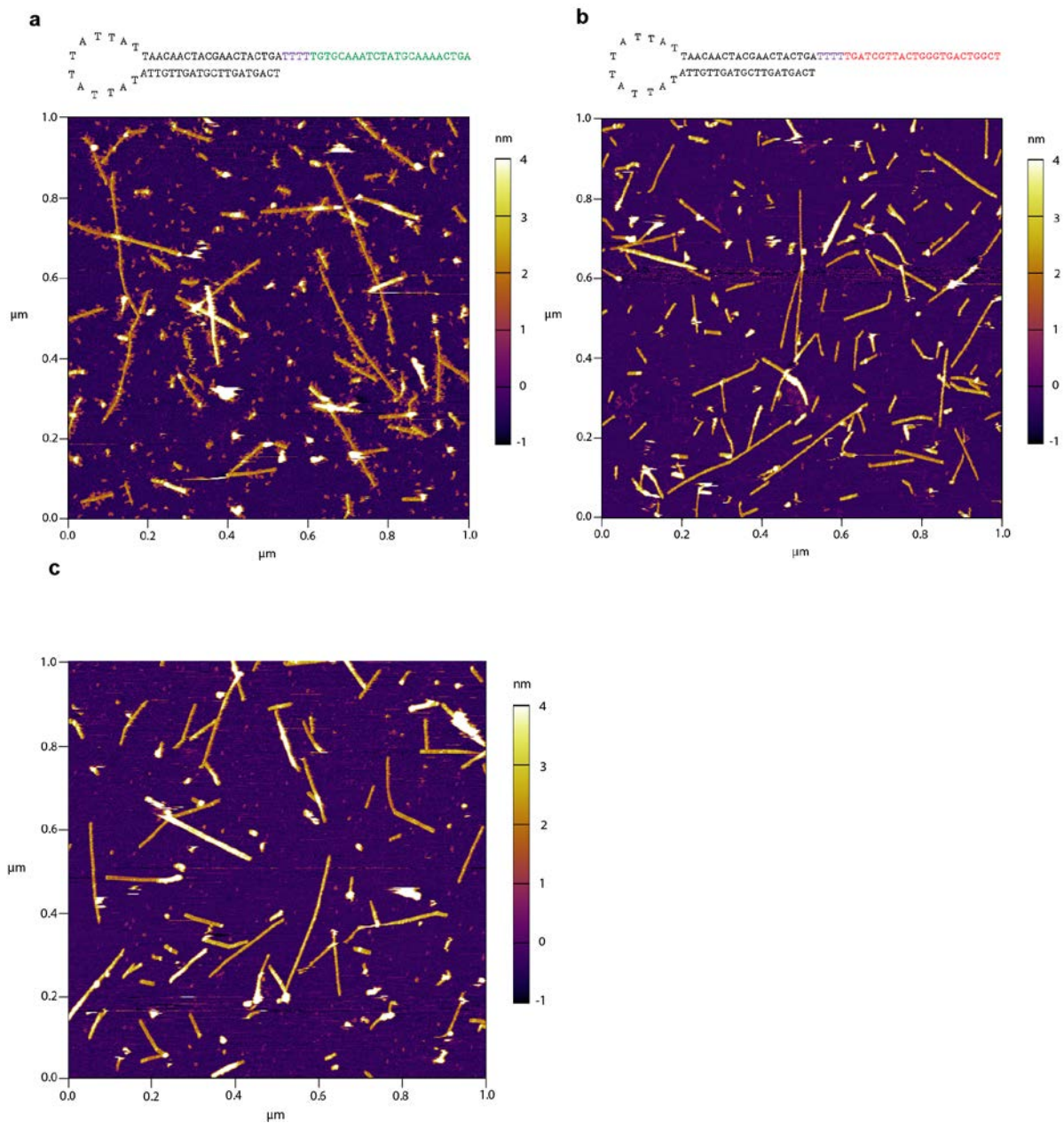


Figure S6. Atomic force microscopy of the GT15mir19 complex under aqueous conditions. **a**, After incubation with miR-19HP, the complementary binding partner. **b**, After incubation with R23HP, a non-complementary control. **c**, After incubation with buffer only.

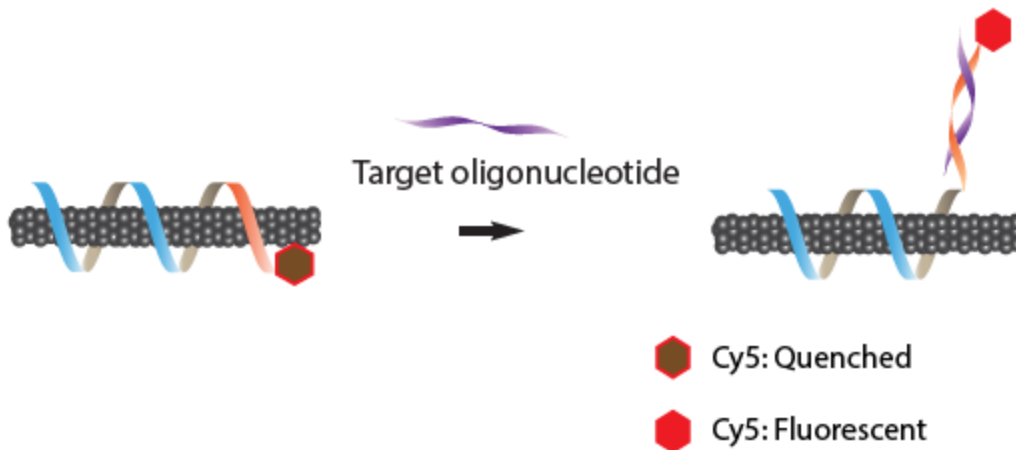


Figure S7. Cartoon depicting the fluorophore dequenching of GT6mir19-Cy5 upon binding of the target miR-19 DNA sequence. A Cy5 dye is conjugated to the 3' end of a sequence composed of $(GT)_6$ and the complementary sequence to miR-19. The Cy5 emission is quenched on the nanotube surface, and fluorescence is expected to be restored if hybridization results in displacement of Cy5 from the nanotube surface.

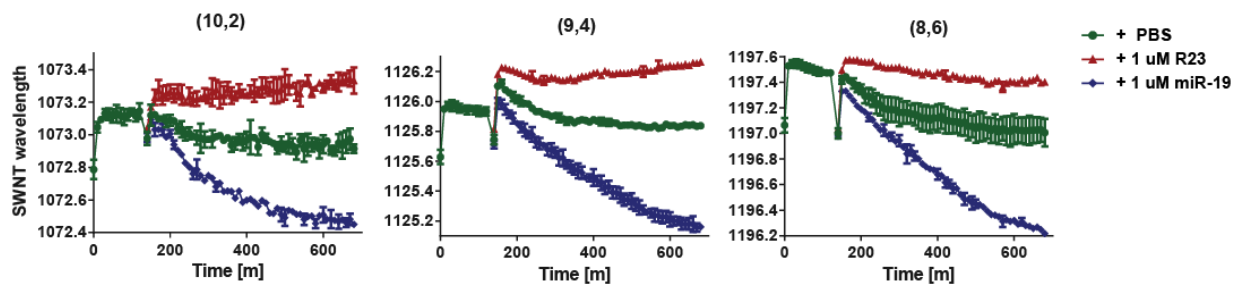


Figure S8. Near-infrared emission wavelength response of the modified sensor complex, GT6mir19-Cy5, used for the fluorophore dequenching experiment. The sensor was interrogated with miR-19 (blue), R23 (red), or buffer only (green). The emission wavelength response of three nanotube chiralities, (10,2), (9,4), and (8,6), are shown. Error bars represent standard error of the mean for $n = 3$ technical replicates.

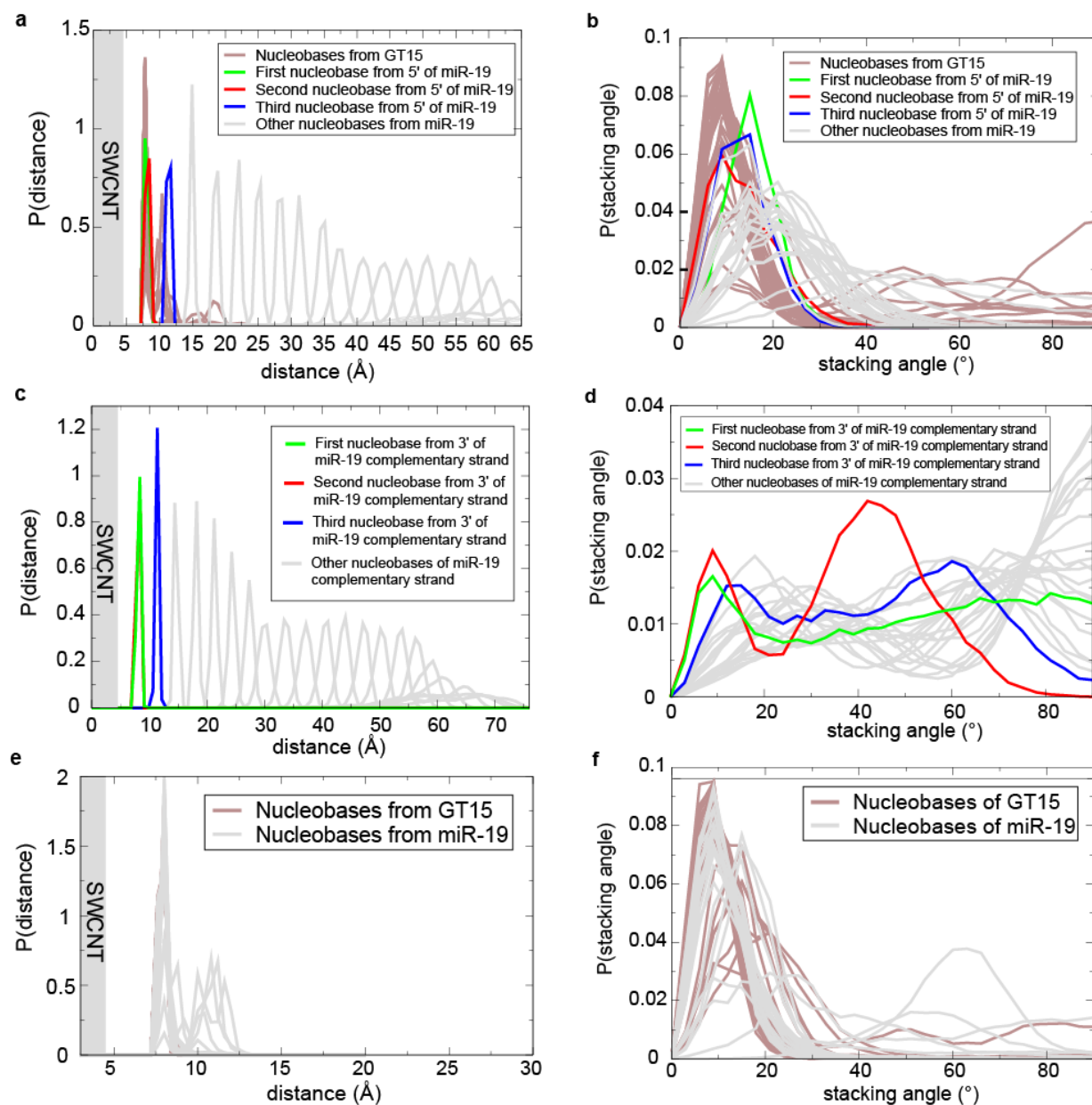


Figure S9. Structural parameters of the GT15mir19 sensor complex computed for the (9,4) nanotube via molecular dynamics simulations. **a**, Distribution of radial distance and **b**, stacking angle relative the nanotube for nucleobases from the GT15 nanotube binding domain and miR-19 miRNA capture sequence domain when hybridized to target miR-19. **c**, Distribution of radial distance and **d**, stacking angle relative to the nanotube for nucleobases from the hybridized target miR-19 when hybridized with the miRNA capture sequence. **e** Distributions of radial distance from the nanotube of the miR-19 miRNA capture sequence when target miR-19 is not hybridized. **f**, Stacking angle of miR-19 miRNA capture sequence when target miR-19 is not hybridized.

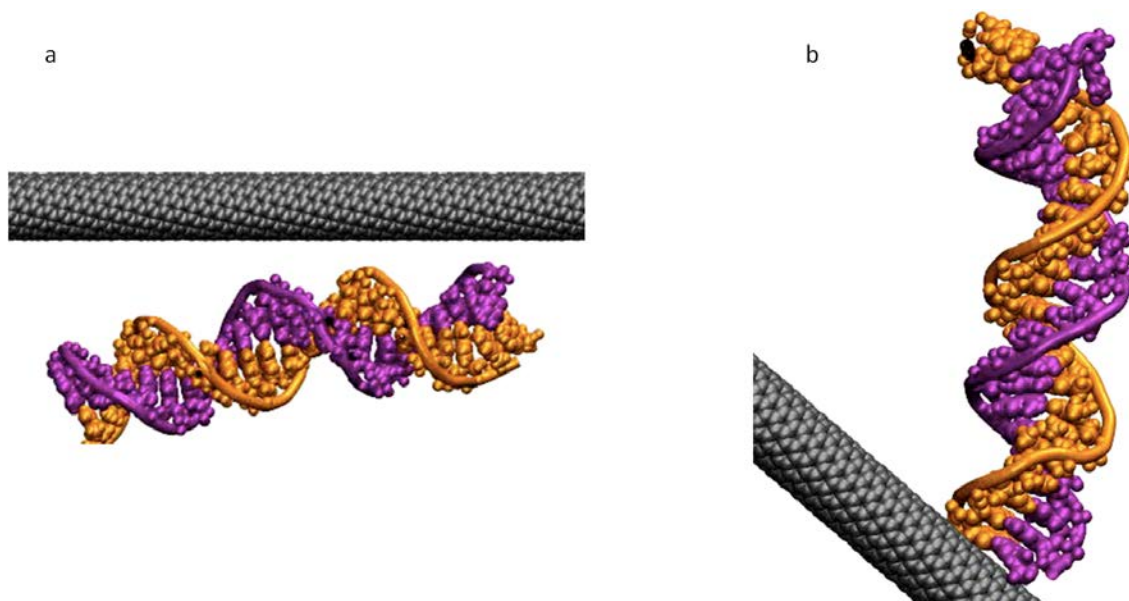
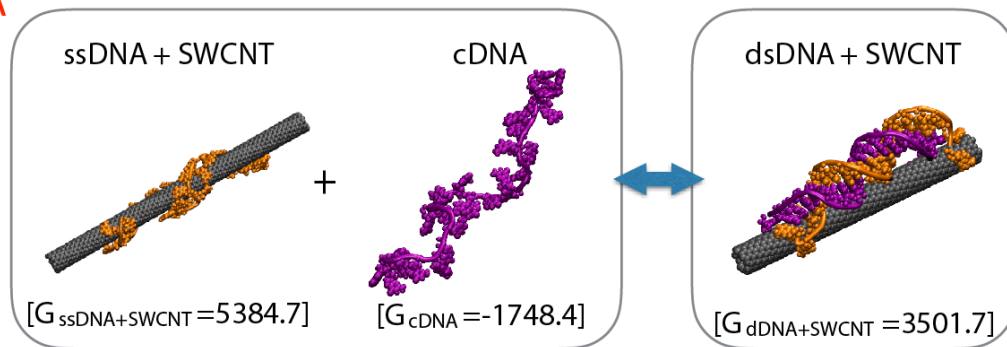


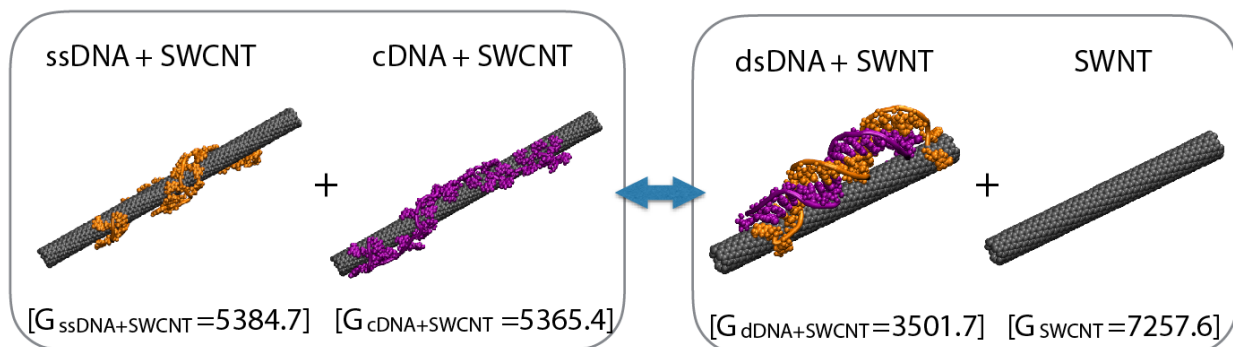
Figure S10. Starting configurations of molecular dynamics simulations involving the duplex miRNA capture sequence + miR-19 without the GT₁₅ nanotube binding domain. **a**, miRNA capture sequence/miR-19 duplex initially configured parallel to the axial vector of the nanotube **b**, miRNA capture sequence/miR-19 duplex initially configured perpendicular to the axial vector of the nanotube.

Case A



$$\Delta G_{\text{hyb on SWCNT}} = G_{\text{dsDNA+SWCNT}} - (G_{\text{ssDNA+SWCNT}} + G_{\text{cDNA}}) = -135 \text{ kcal/mol}$$

Case B



$$\Delta G_{\text{hyb on SWCNT}} = (G_{\text{dsDNA+SWCNT}} + G_{\text{SWCNT}}) - (G_{\text{ssDNA+SWCNT}} + G_{\text{cDNA}}) = 9 \text{ kcal/mol}$$

Figure S11. Two calculations of hybridization free energy of DNA on the nanotube surface. Graphics are illustrative examples of the reference states and G_{binding} values are taken the work by Jung et al. (ref 7)

Case A depicts the scenario where single stranded DNA on a nanotube hybridizes with complementary DNA in solution. **Case B** depicts the scenario where both strands are first adsorbed to the nanotube surface.

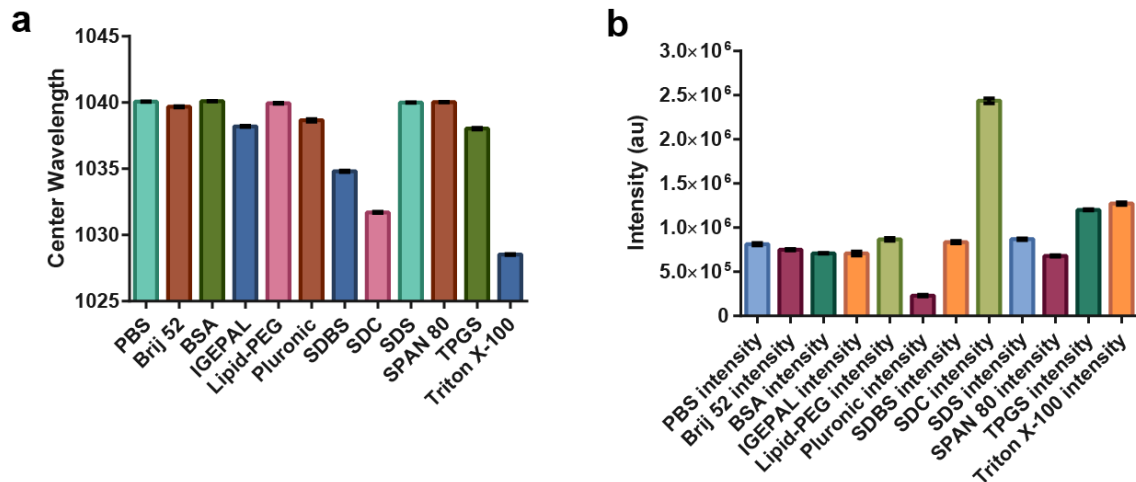


Figure S12: **a**, Mean peak wavelength and **b**, intensity values of the GT15mir19 complex after incubation with amphiphilic molecules. Data is shown for the (7,5) nanotube species. Error bars represent standard deviation from three technical replicates.

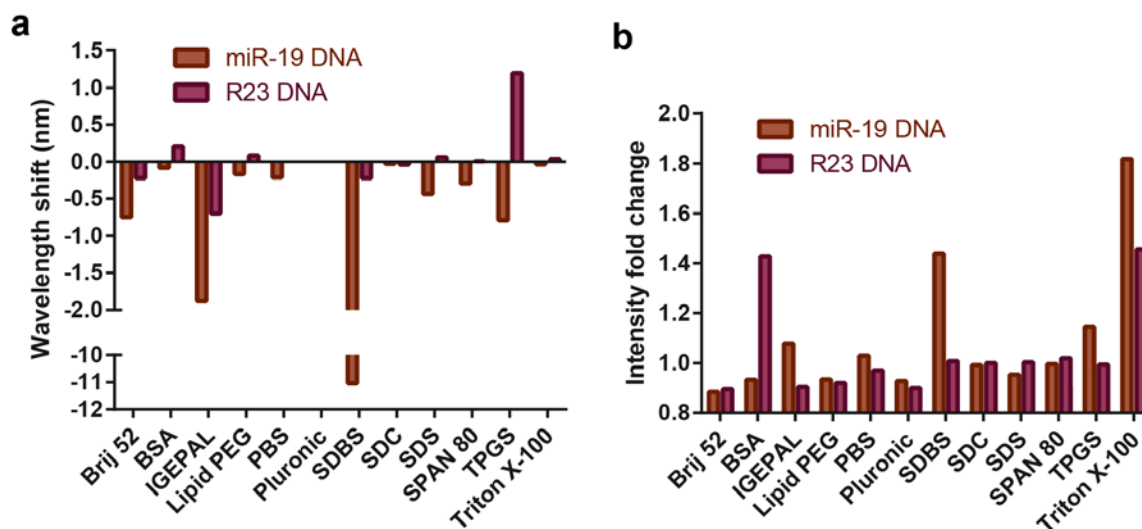


Figure S13: Change of the GT15mir19 sensor response to miRNA upon interrogation with a panel of amphiphilic molecules. **a**, Wavelength shift from buffer control and **b**, intensity fold enhancement over buffer control are shown following incubation with the target oligonucleotide or non-complementary control after 4 hours.

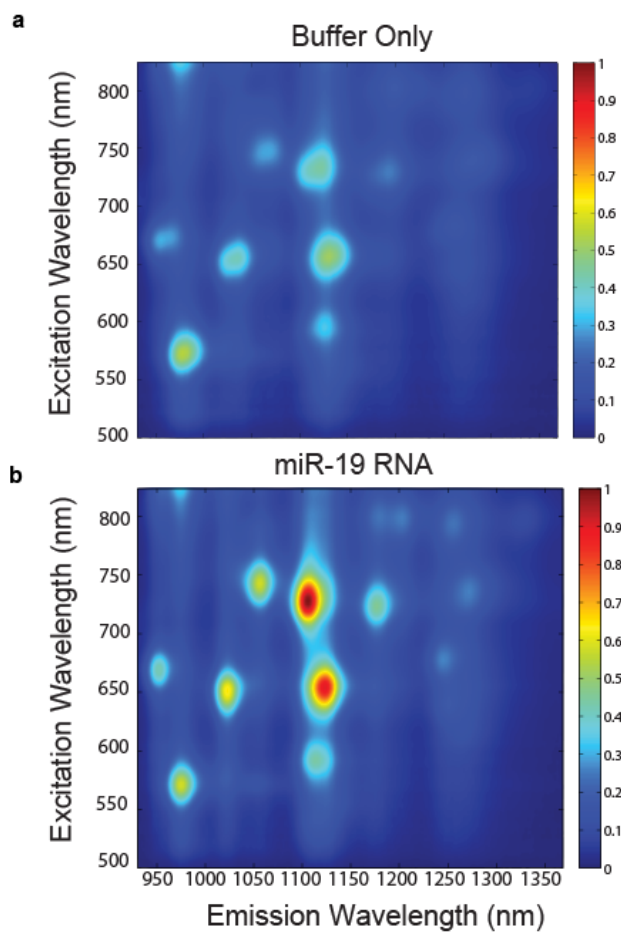


Figure S14. Photoluminescence excitation/emission plots of the GT15mir19 sensor with 0.2% SDBS. **a**, Buffer only control. **b**, After incubation with miR-19 RNA.

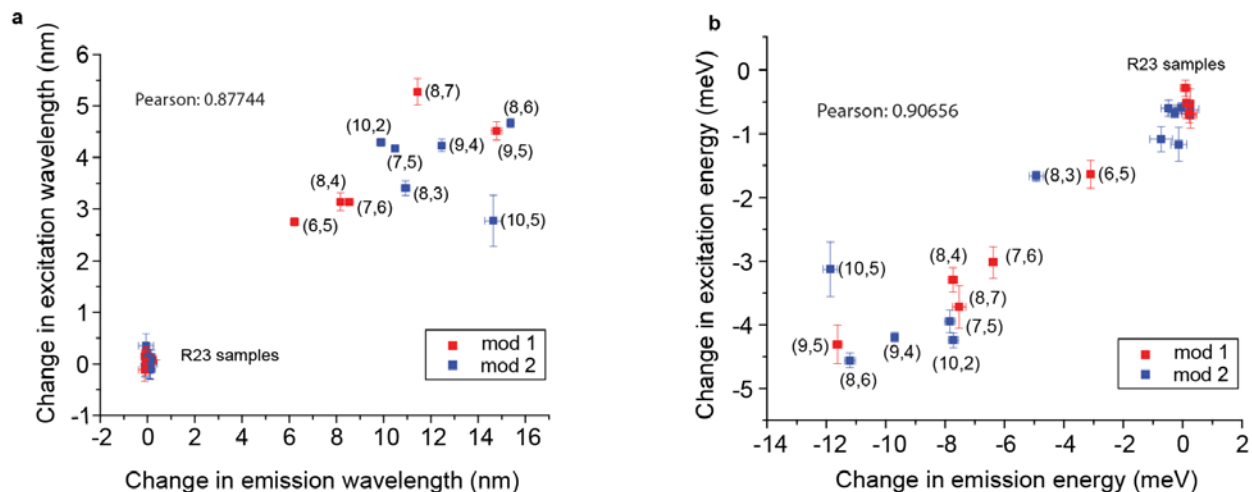


Figure S15. Excitation and emission wavelength shifts of the GT15mir19 sensor, calculated from photoluminescence excitation/emission (PL) plots. **a**, Absolute wavelength shifts of the sensor upon introduction of miR-19 RNA or random sequence RNA control (R23). **b**, Change in excitation and emission energy in response to miR-19 RNA or random sequence RNA control (R23). Red = nanotube chiralities that satisfy $(2n+m) \bmod 3 = 1$ (mod 1). Blue = nanotube chiralities that satisfy $(2n + m) \bmod 3 = 2$ (mod2). The Pearson correlation coefficient for the x vs. y values of each graph is indicated. Error bars represent standard error of the mean for $n = 3$ technical replicates.

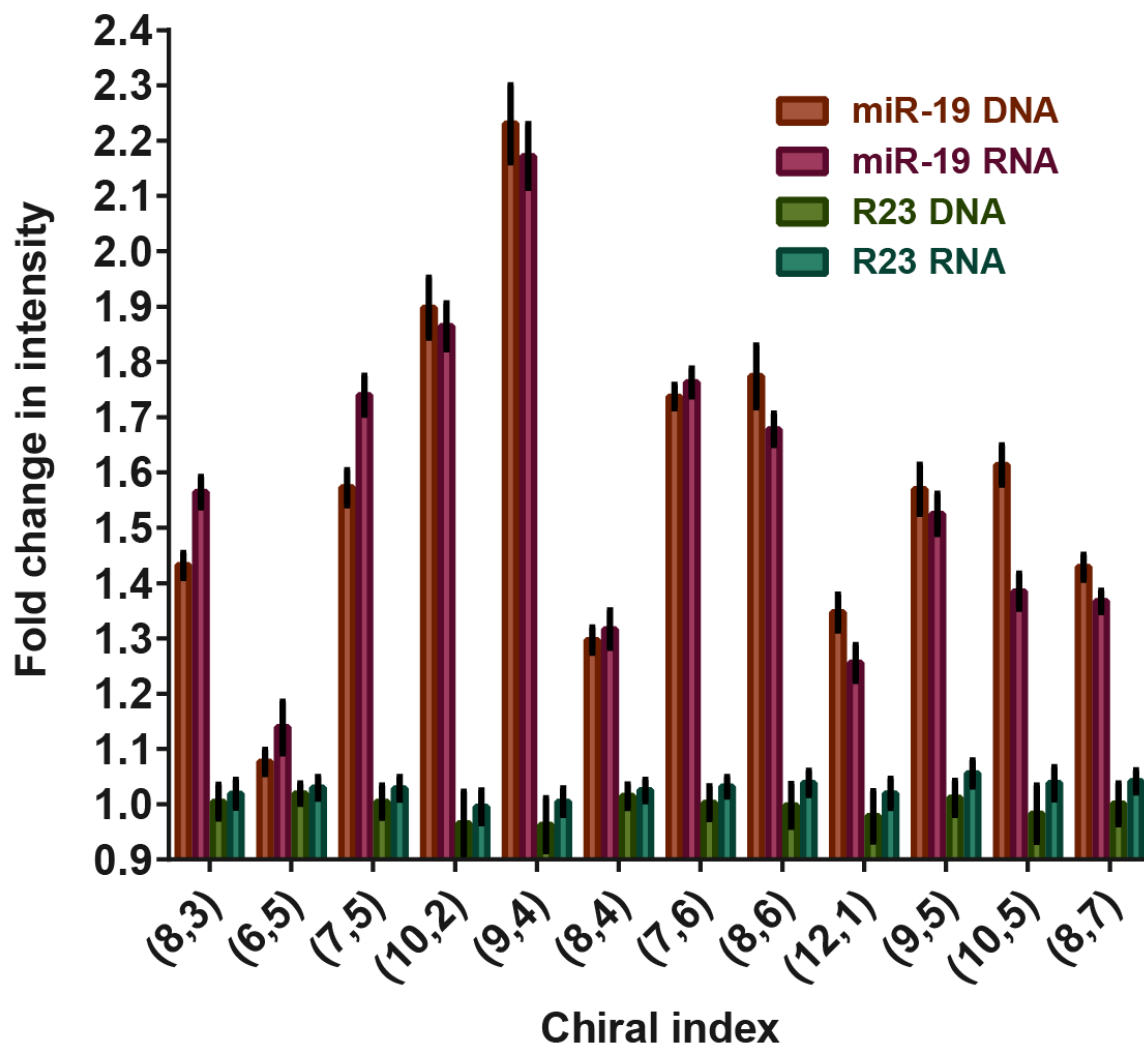


Figure S16. Change in intensity of the GT15mir19 sensor in the presence of 0.2% SDBS. Intensity was calculated from photoluminescence excitation/emission plots and normalized to buffer only control. Error bars represent standard error of the mean for n = 3 technical replicates.

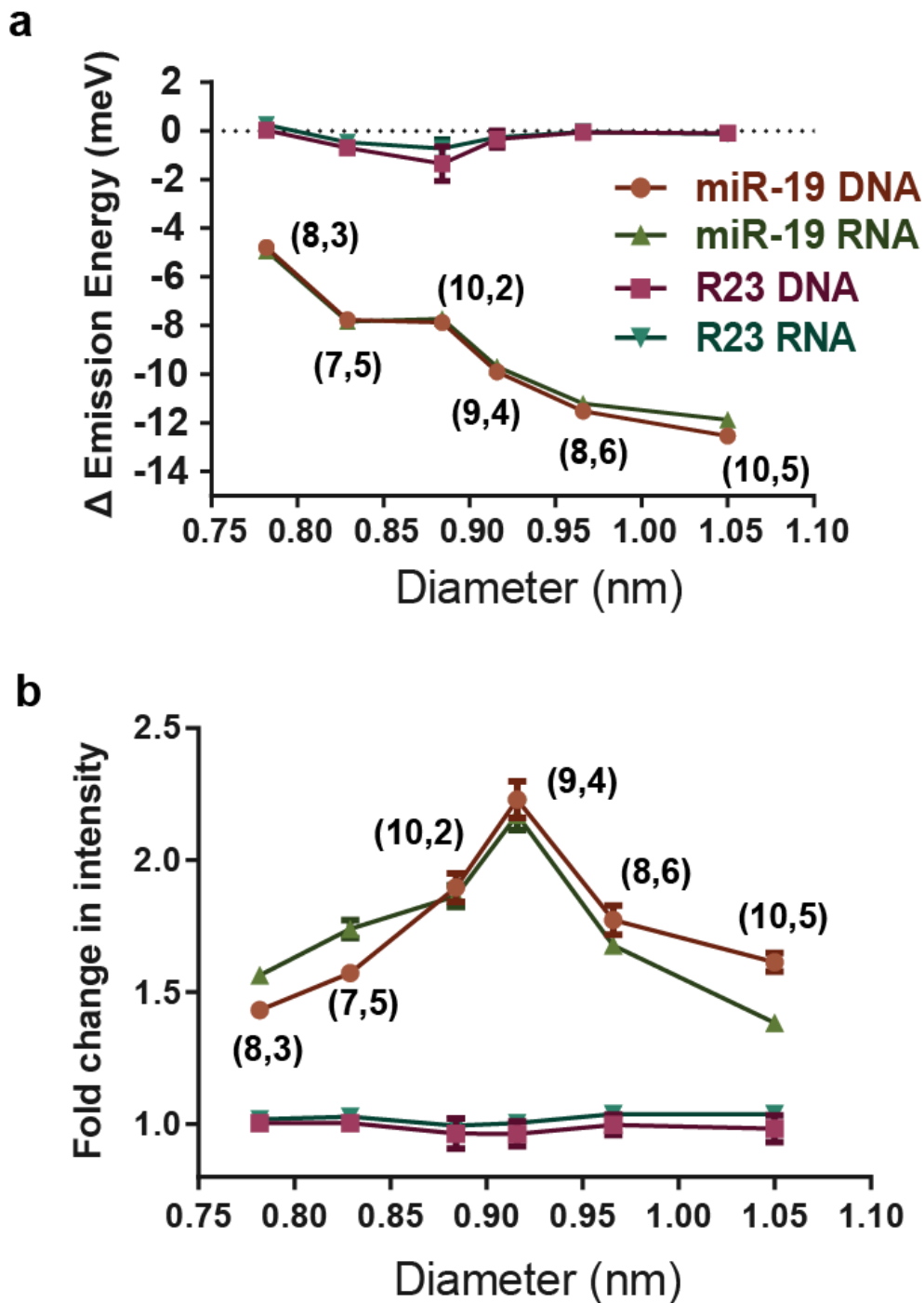


Figure S17. Diameter dependence of emission energy change and intensity change. **a**, Change in emission energy of the GT15mir19 sensor as a function of nanotube diameter, for mod2 nanotubes. **b**, Change in GT15mir19 sensor emission intensity, as a function of nanotube diameter, for mod 2 nanotubes. Error bars represent standard error of the mean for $n = 3$ technical replicates.

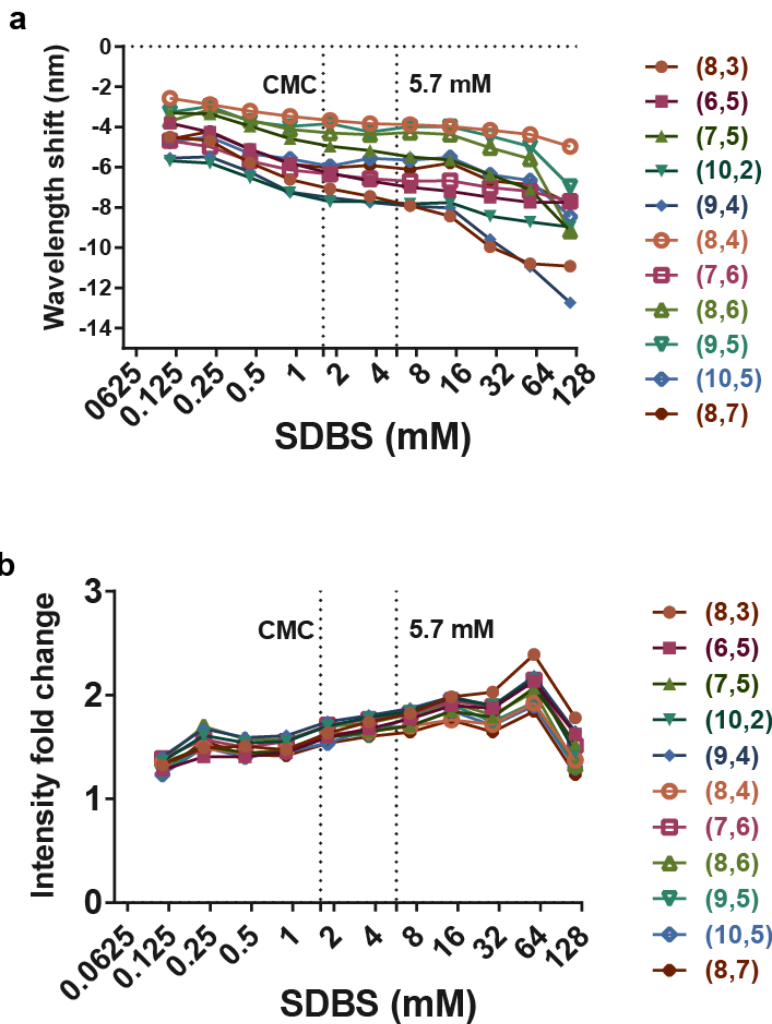


Figure S18. Emission response of the GT15mir19 sensor to different SDBS concentrations, in the absence of analyte. **a**, Emission wavelengths of 11 nanotube chiralities after an overnight incubation with SDBS. **b**, Intensity change in response to SDBS. Dotted lines indicate critical micelle concentration (CMC, 1.6 mM), and the concentration of SDBS used in most experiments of this work (5.7 mM, 0.2% w/v).

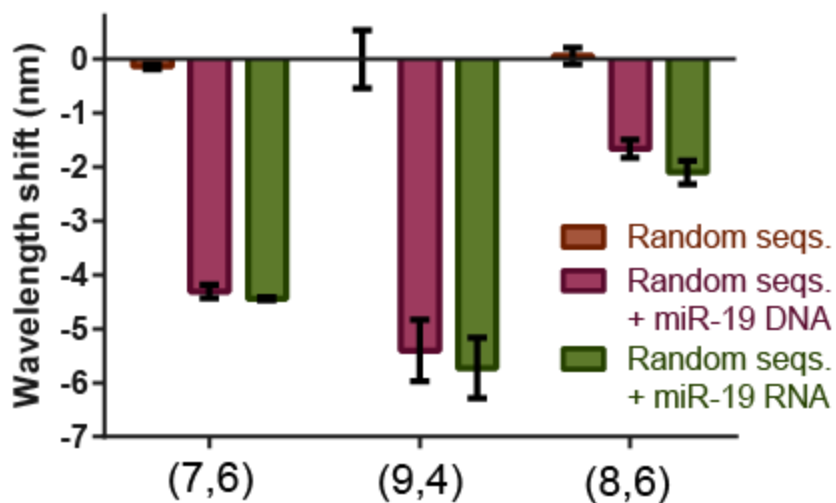


Figure S19. Wavelength response of the GT15mir19 sensor in the presence of random permutations of DNA 23 nucleotides in length (random seqs.) alone, random seqs. with miR-19 DNA, and random seqs. with miR-19 RNA. The responses of three different nanotube chiralities are shown. Error bars represent standard error of the mean for $n = 3$ technical replicates.

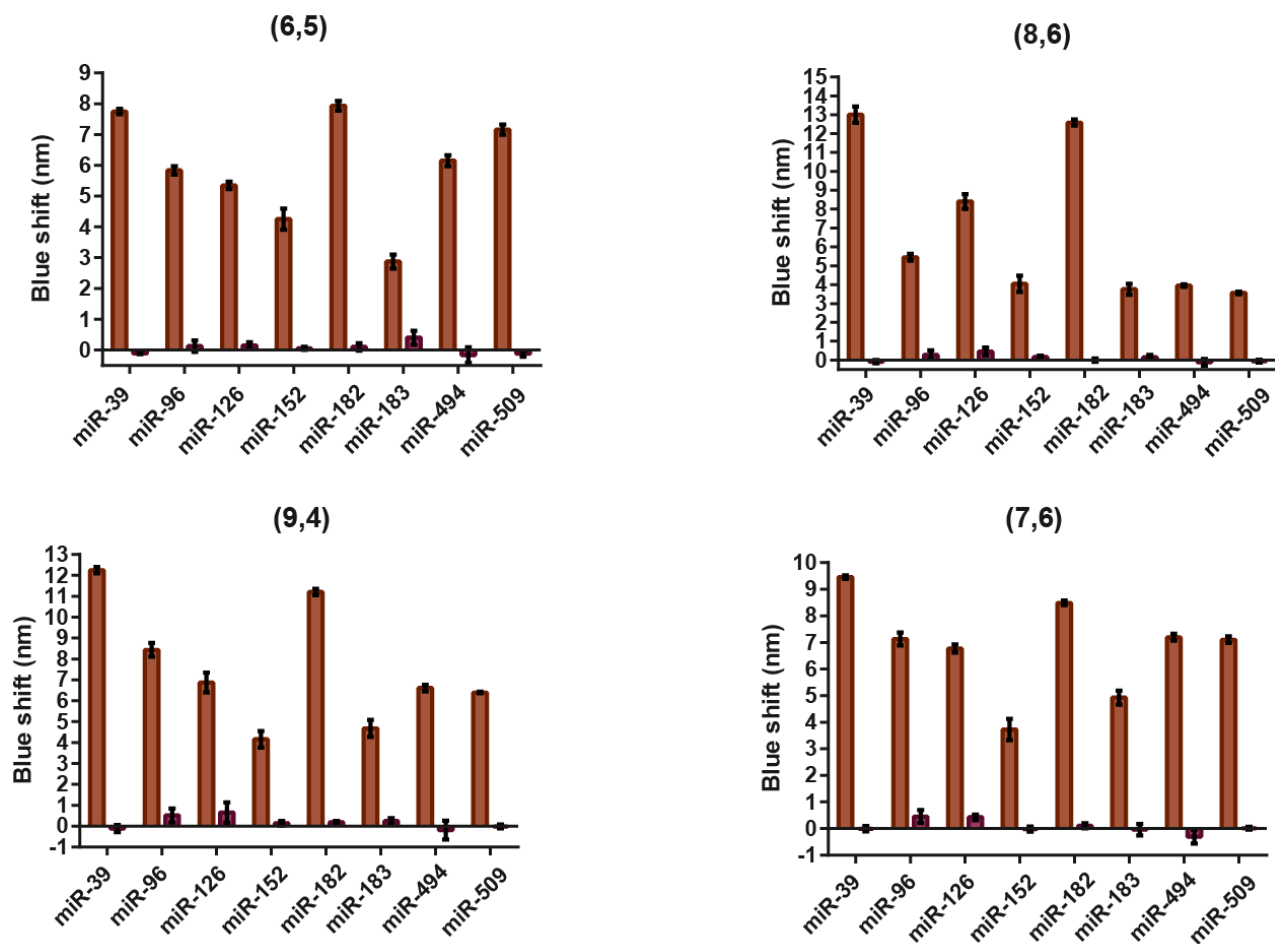


Figure S20: Emission wavelength response of GT15mirX sensors to their complementary miR biomarker sequence or R23 non-complementary control (DNA). The responses of four nanotube chiralities are shown. Error bars represent standard error of the mean for $n = 3$ technical replicates.

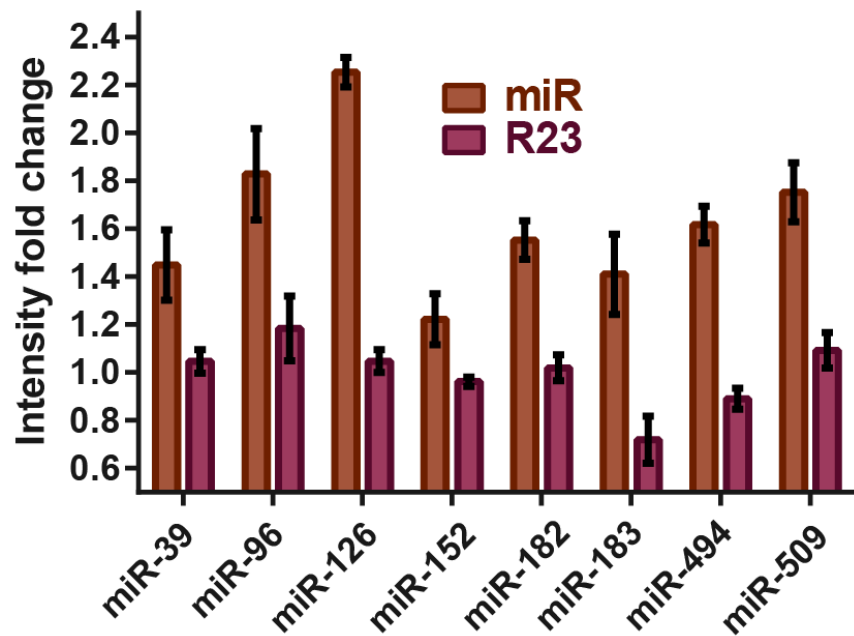


Figure S21: Intensity response of the GT15mirX sensors after the introduction of target miR sequences or R23 non-complementary control. The response of the (7,5) nanotube is shown, normalized to the buffer only control. Error bars represent standard error of the mean for $n = 3$ technical replicates.

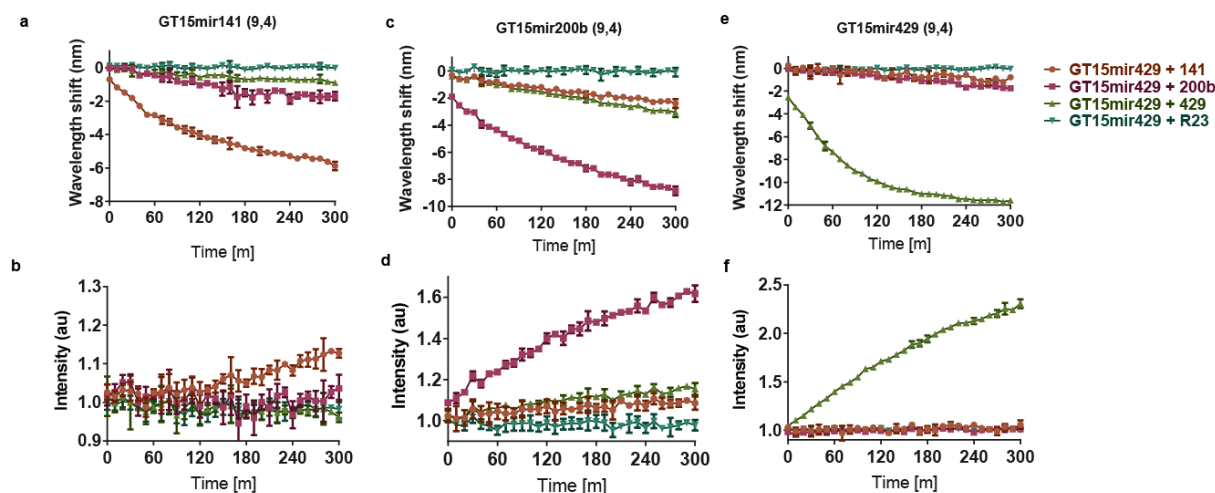


Figure S22. Kinetic response of the GT15mirX sensor to three closely-related sequences. The response of the (9,4) chirality is shown. **a** and **b**, wavelength shift and intensity change of the sensor specific for miR-141 (GT15mir141). **c** and **d**, wavelength shift and intensity change over time for sensor specific for miR-200b (GT15mir200b). **e** and **f**, wavelength shift and intensity fold change over time for sensor specific for miR-429 (GT15mir429). Error bars represent standard error of the mean for $n = 3$ technical replicates.

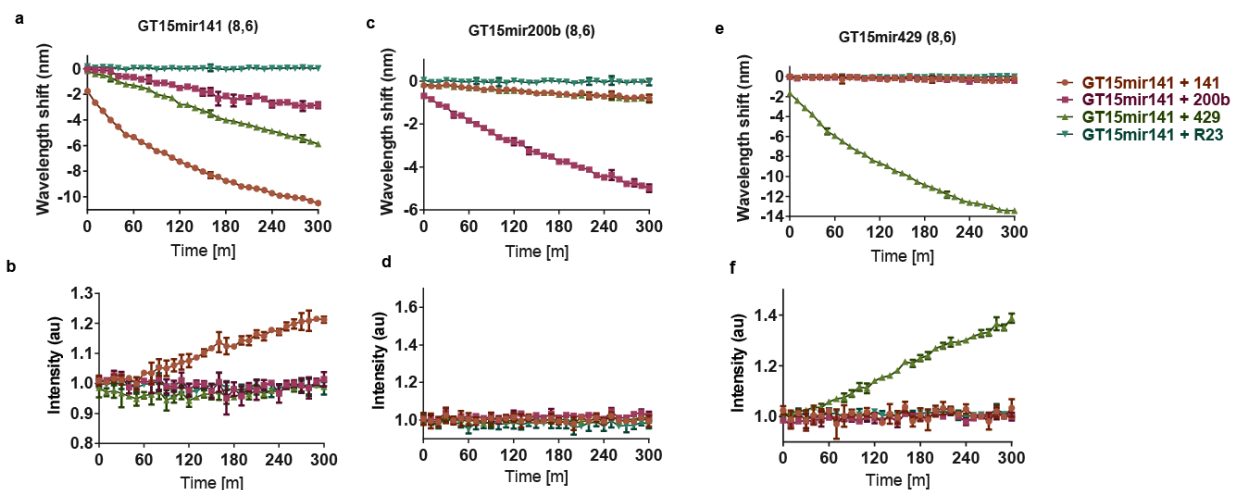
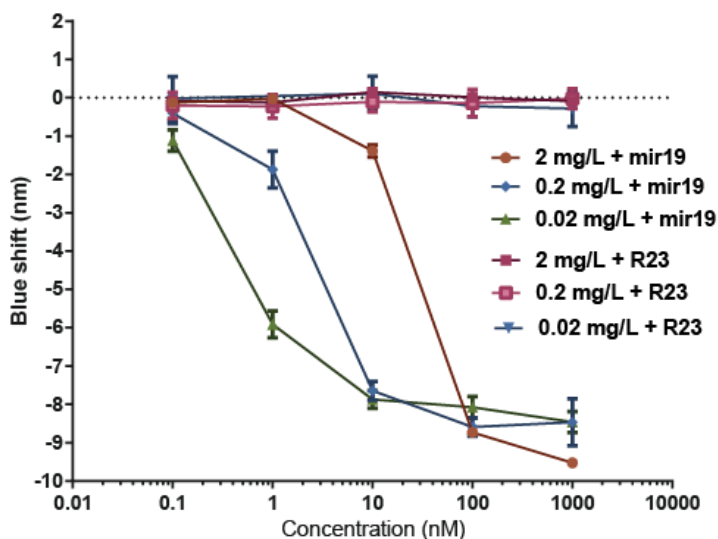


Figure S23. Kinetic response of the GT15mirX sensor to three closely-related sequences. The response of the (8,6) chirality is shown. **a** and **b**, wavelength shift and intensity fold change over time for sensor specific for miR-141 (GT15mir141). **c** and **d**, wavelength shift and intensity fold change over time for sensor specific for miR-200b (GT15mir200b). **e** and **f**, wavelength shift and intensity fold change over time for sensor specific for miR-429 (GT15mir429). Error bars represent standard error of the mean for $n = 3$ technical replicates.



SWCNT conc.	LOD	Binding sites	Saturating range
2 mg/L	1 nM to 10 nM	211.7 nM	100-1000 nM
0.2 mg/L	100 pM to 10 nM	21.17 nM	10-100 nM
0.02 mg/L	10 pM to 100 pM	2.117 nM	1-10 nM

Figure S24. Dose-response curves of the GT15mir19 sensor response, using three different sensor concentrations. Table indicates observed limit of detection (LOD), calculated number of binding sites, and measured saturating range of the sensor. Error bars represent standard error of the mean for $n = 3$ technical replicates.

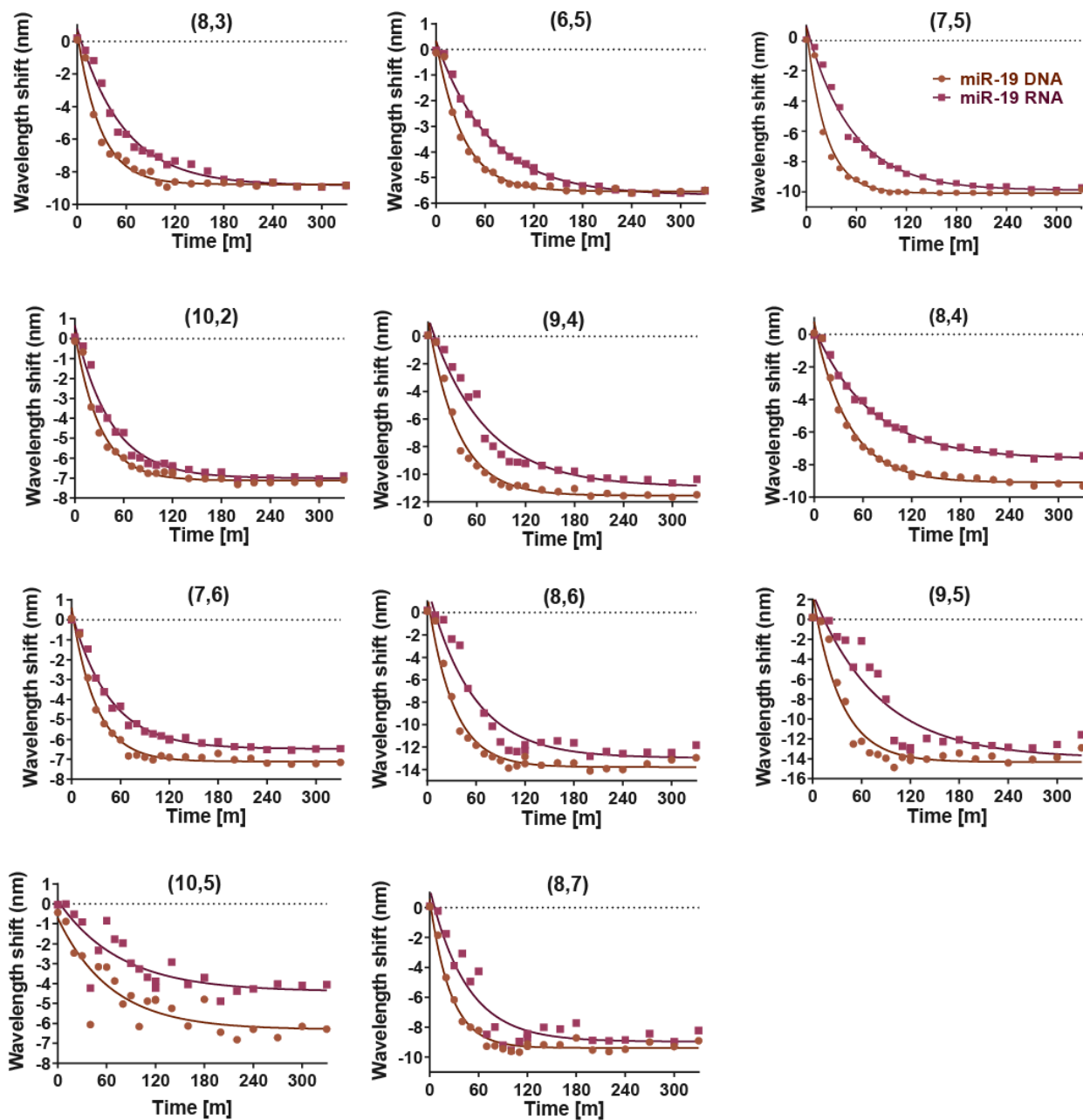


Figure S25. Kinetic data for all measured chiralities of the GT15mir19 sensor after addition of miR-19 DNA or miR-19 RNA. Data was acquired in 10-minute intervals. All data is fitted to an exponential decay, $y = y_0 e^{-kt}$.

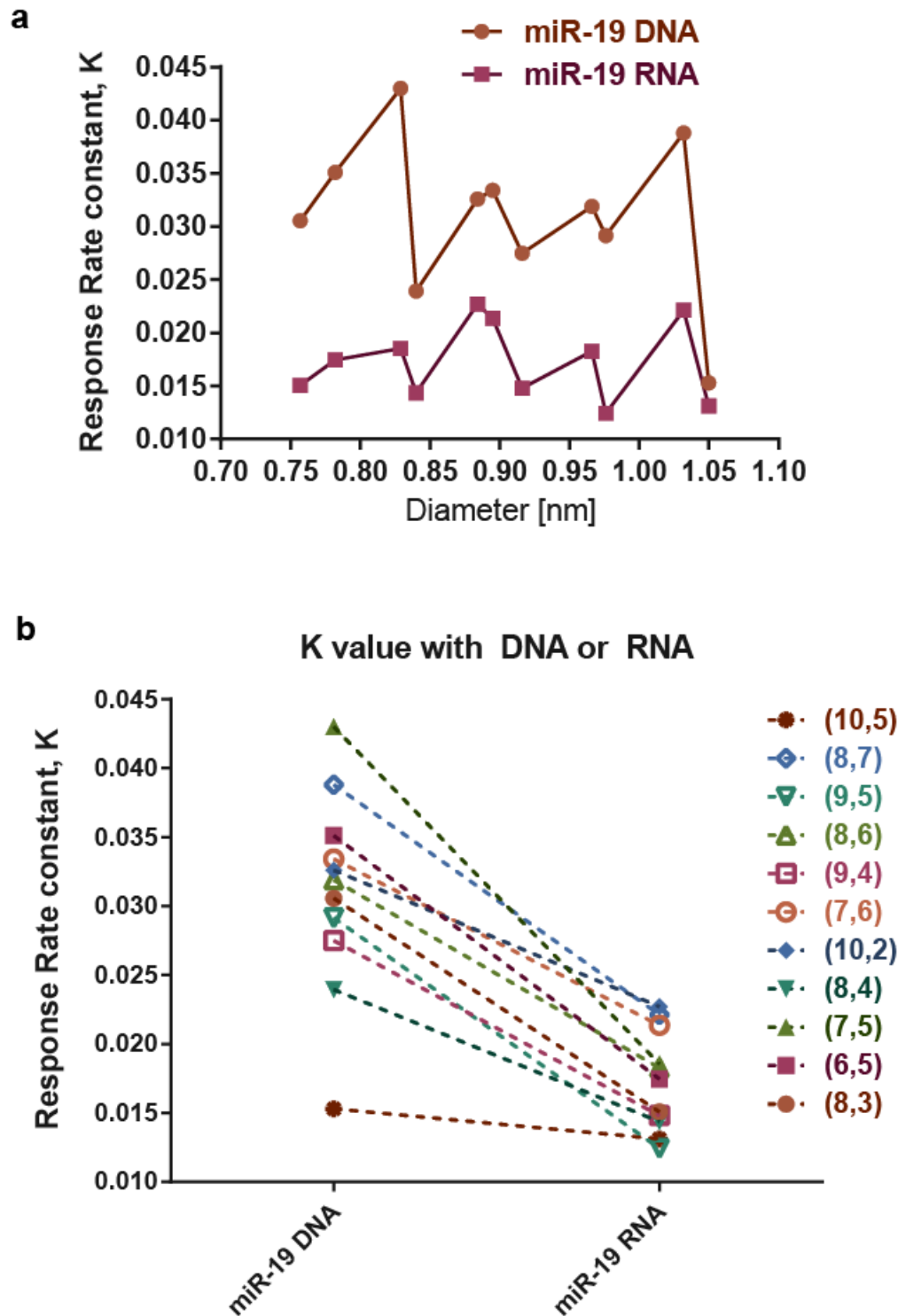


Figure S26. Comparison of the response rate of the GT15mir19 sensor to DNA or RNA versions of the target, for eleven different nanotube chiralities **a**, Rate constant K of the GT15mir19 wavelength response after addition of miR-19 DNA or RNA, arranged according to nanotube diameter. **b**, Comparison of rate constants of each nanotube chirality, in response to miR-19 DNA and miR-19 RNA.

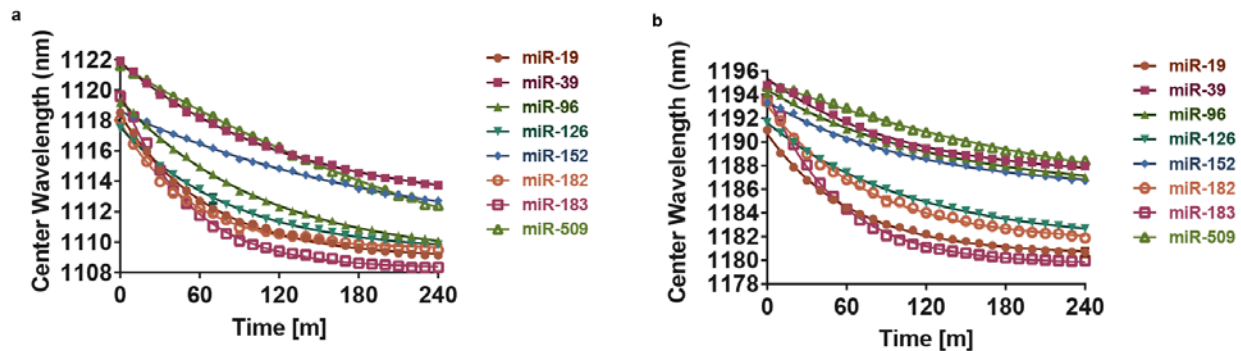


Figure S27. Kinetics of the wavelength response of GT15mirX sensors after addition of target miR biomarker sequences. **a**, Response of the (9,4) nanotube chirality. **b**, Response of the (8,6) nanotube chirality. Smooth curves are fitted exponential decays, $y = y_0 e^{-kt}$.

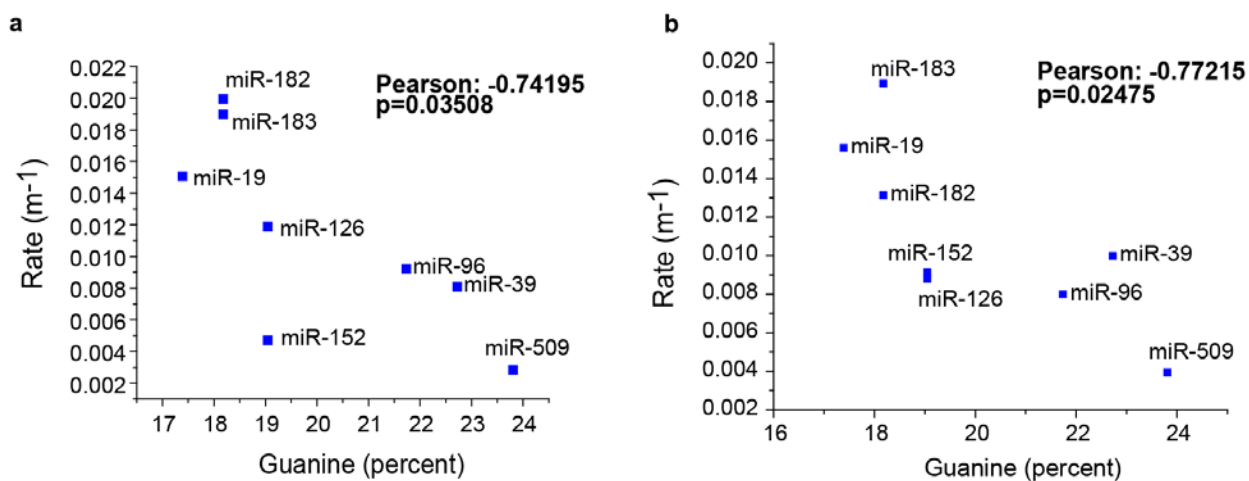


Figure S28. GT15mirX sensor response rates vs. guanine content of the miRNA capture sequences. **a**, Response of the (9,4) nanotube chirality. **b**, Response of the (8,6) nanotube chirality. Pearson correlation coefficients are indicated.

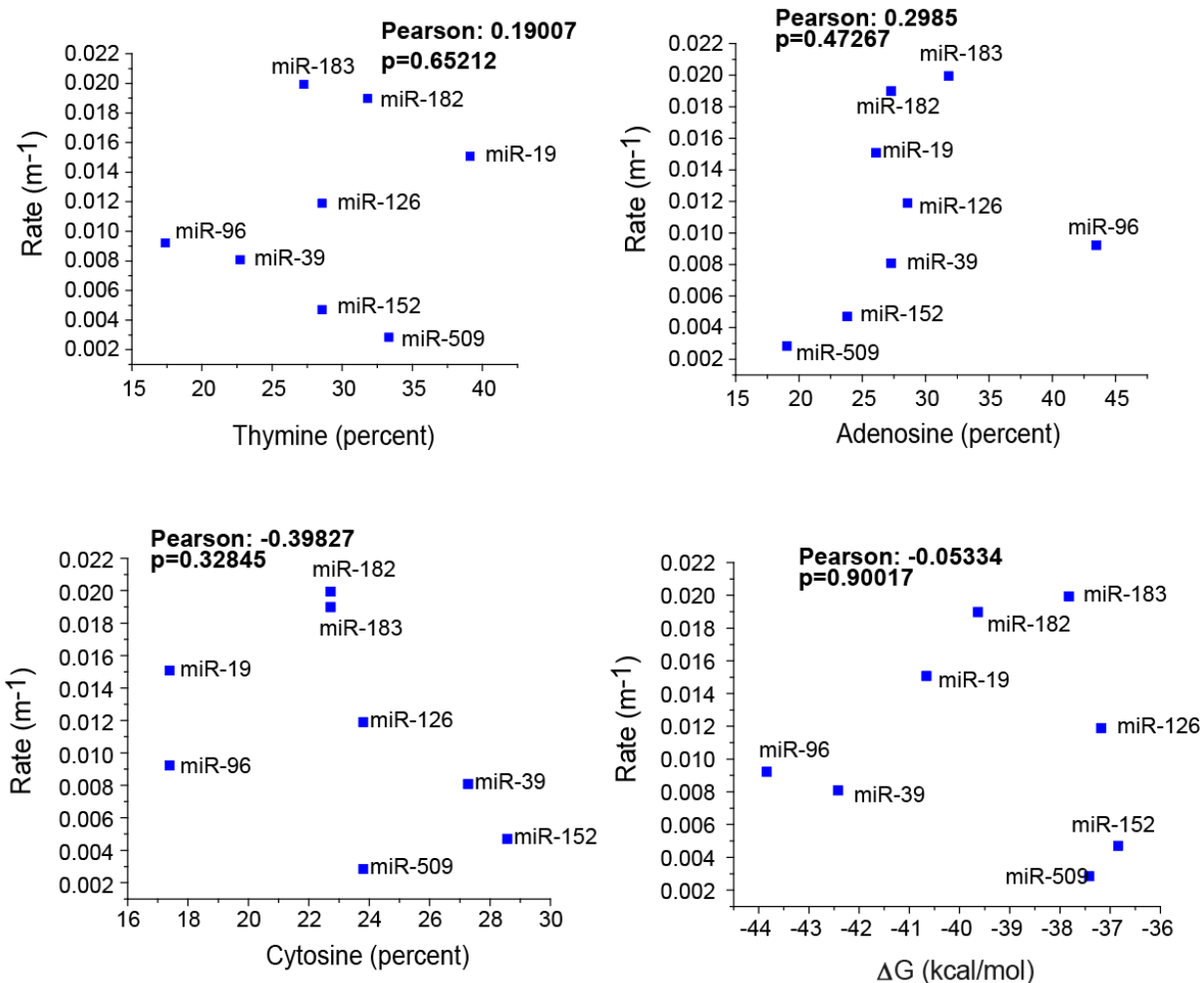


Figure S29. GT15mirX sensor response rates vs. thymine, adenosine, and cytosine content of the miRNA capture sequence, or free energy of hybridization of the miRNA capture sequence. Response of the (9,4) chirality was measured. No statistically significant correlations were found.

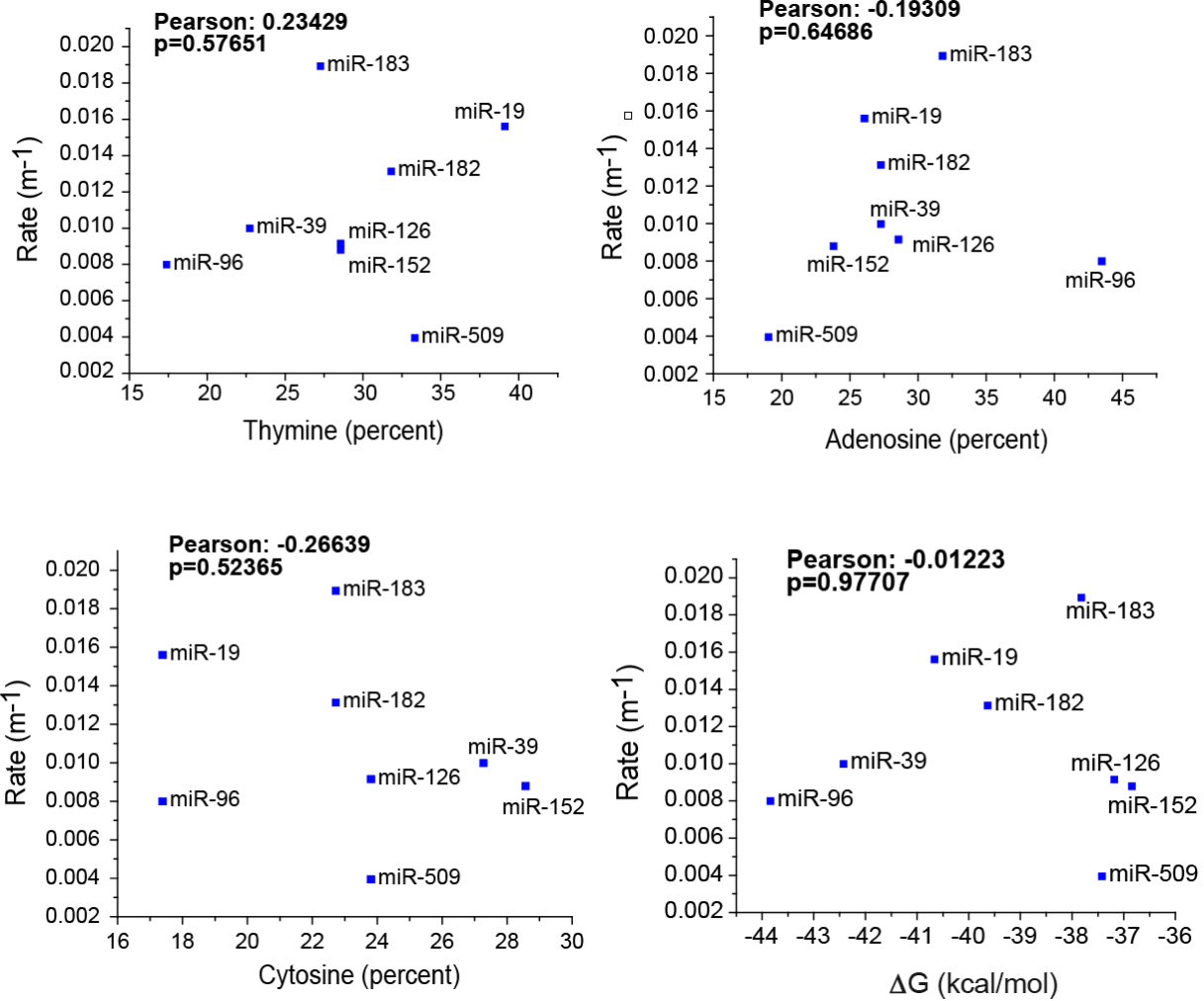


Figure S30. GT15mirX sensor response rates vs. thymine, adenosine, and cytosine content of the miRNA capture sequence, or free energy of hybridization of the miRNA capture sequence. Response of the (8,6) chirality was measured. No statistically significant correlations were found.

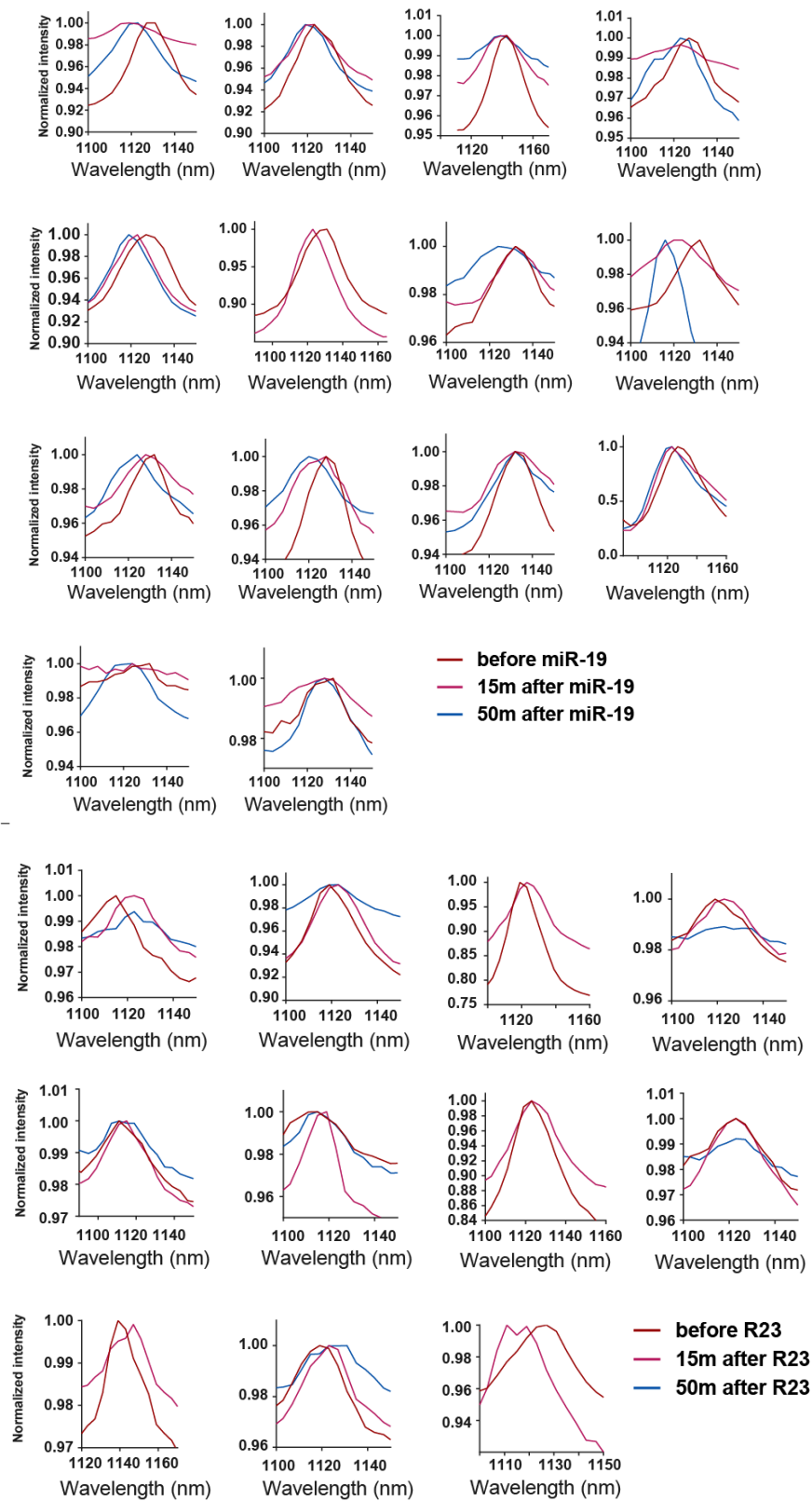


Figure S31. Single-GT15mir19 spectra measured via near-infrared hyperspectral microscopy, before addition of miR-19 RNA or R23 RNA, 15 minutes after addition, and 50 minutes after addition.

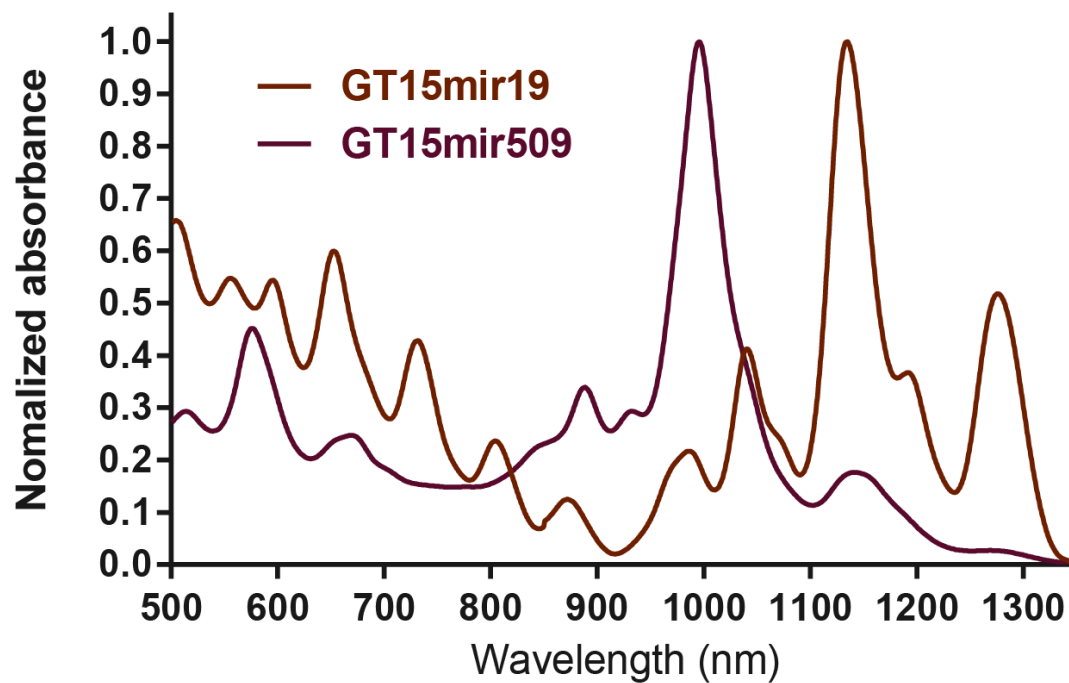


Figure S32. Normalized absorbance spectra of GT15mir19 oligonucleotide-suspended APT-200 from Nano-C and GT15mir509 oligonucleotide-suspended CoMoCAT SG65i grade.

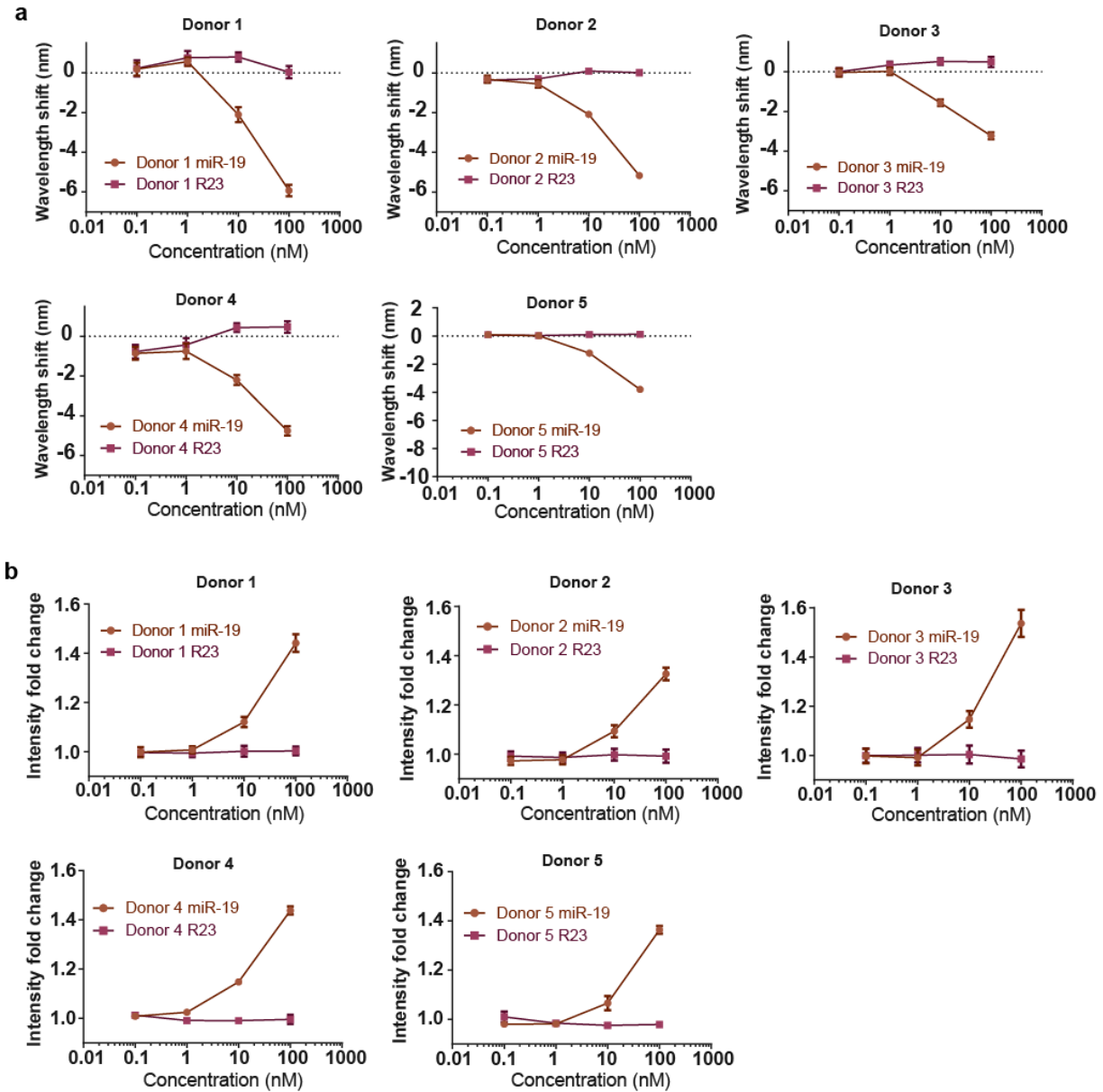


Figure S33. Sensor response in urine from healthy donors. **a**, Wavelength shift as a function of miR-19 RNA or non-complementary control R23 concentration for each individual donor. **b**, Intensity fold enhancement as a function of added miR-19 RNA or non-complementary control R23 concentration. Error bars represent standard deviation of three technical replicates.

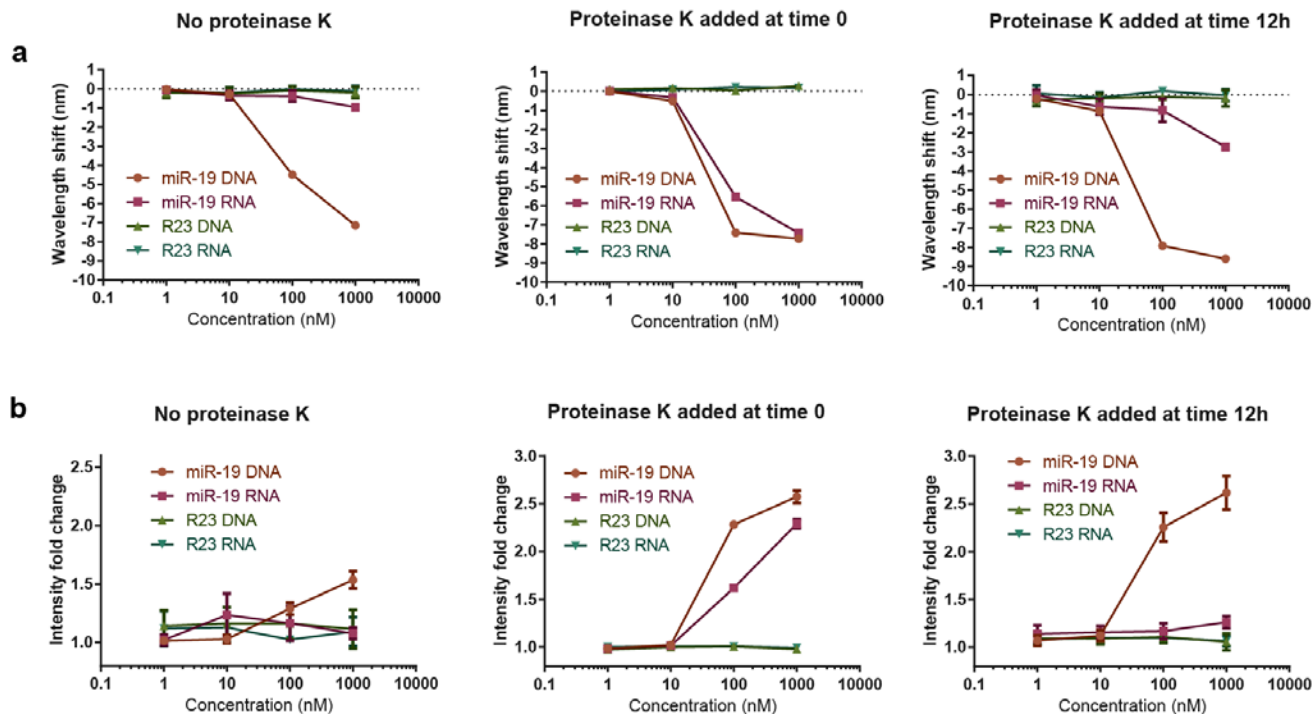


Figure S34. Study of the sensor response in serum. **a**, Wavelength shift of the GT15mir19 sensor in whole serum with 0.2% SDBS and upon addition of proteinase K. The response of the (8,6) nanotube is shown. **b**, Intensity change in the same conditions. Error bars represent standard deviation of three technical replicates.

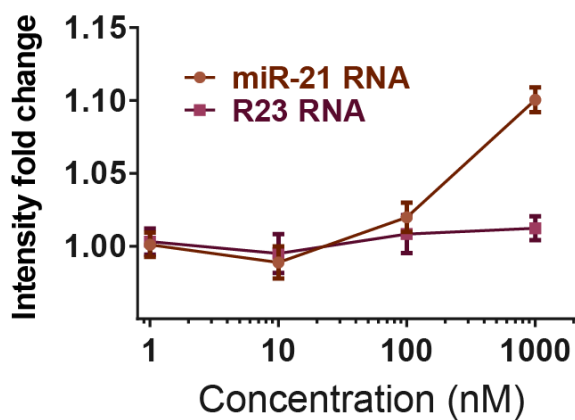


Figure S35: Intensity response of the GT15mir21 sensor after introducing the miR-21 RNA oligonucleotide in serum with proteinase K. Error bars represent standard deviation of three technical replicates.

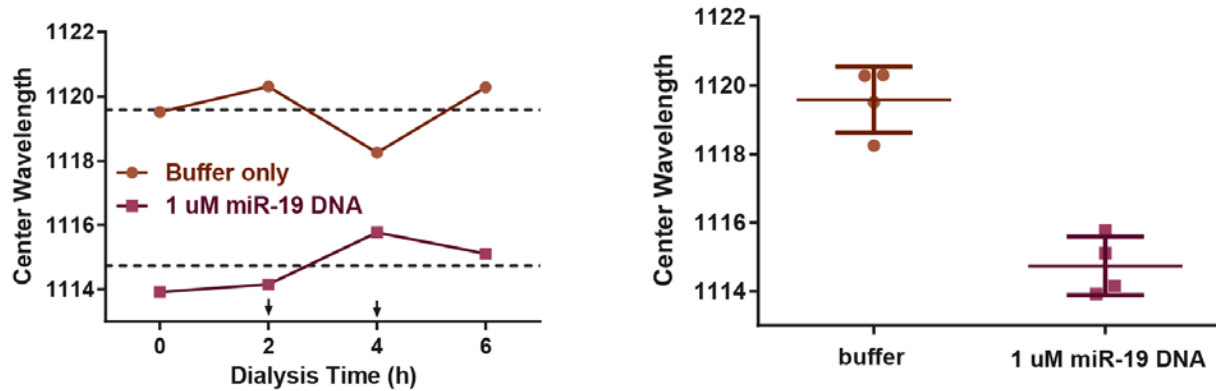


Figure S36. Persistence of wavelength shifting of the GT15mir19 sensor upon dialysis of SDBS. **a**, Emission wavelength response of the sensor, interrogated after the indicated dialysis time. Buffer changes are indicated by the arrows. **b**, Average emission wavelength the sensor in response to miR-19 DNA and buffer control at all timepoints.

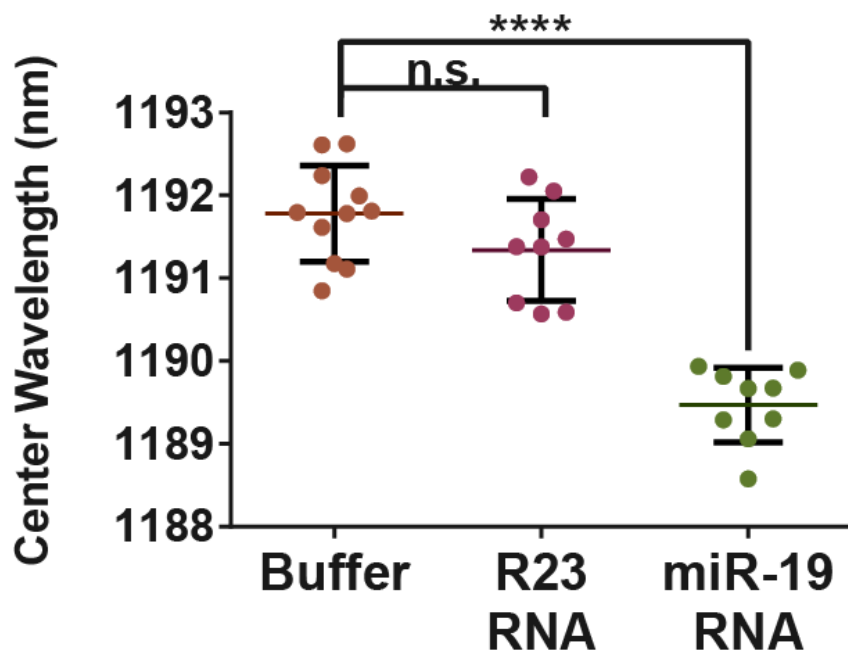


Figure S37: Response of the implanted sensor device to 1 nanomole of miR-19 RNA within live mice. The (8,6) nanotube chirality was measured; 3-4 spectra per animal were taken; 3 animals were measured per group ($p < 0.0001$, Dunnett's multiple comparison test, ordinary one-way ANOVA).

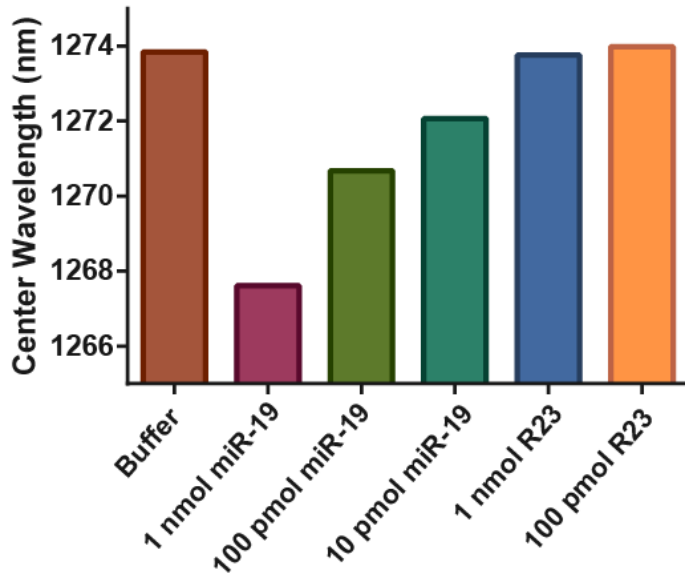


Figure S38. Dose-response curve of the GT15mir19 sensor capillary device measured in vitro.

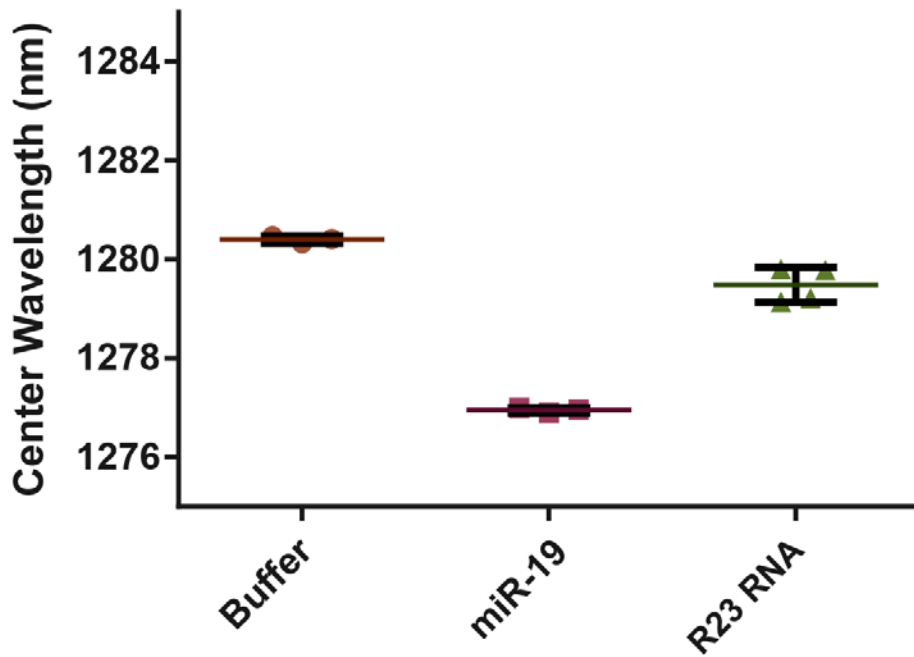


Figure S39: Emission from the implantable devices removed from one animal in each group after injection of buffer, 500 pmol miR-19 RNA, or 500 pmol R23 RNA. Error bars represent standard error of the mean for 3-4 measurements.

Supplementary Tables

Name	Abbreviation	Class of amphipathic molecule
Sodium deoxycholate	SDC	ionic surfactant
Sodium dodecyl sulfate	SDS	ionic surfactant
Sodium dodecylbenenesulfonate	SDBS	ionic surfactant
Pluronic F-68	Pluronic	non-ionic triblock copolymers
Triton X-100	n/a	non-ionic surfactant
IGEPAL CO-530	IGEPAL	non-ionic surfactant
Span 80	n/a	non-ionic surfactant
Brij 52	n/a	non-ionic surfactant
D- α -Tocopherol polyethylene glycol 1000 succinate	TPGS	non-ionic surfactant (vitamin E)
1,2-distearoyl-sn-glycero-3-phosphoethanolamine-N-[methoxy(polyethylene glycol)-1000] (ammonium salt)	Lipid-PEG	PEGylated lipid
Bovine serum albumin	BSA	protein

Table S1: List of amphipathic molecules used to study the enhancement of the sensor response.

Name	Sequence (5' to 3')
GT15mir19	GTGTGTGTGTGTGTGTGTGTGTGTGTGTGTGTGTTTCAGTTTTGCATAGATTTGCACA
GT15mir126	GTGTGTGTGTGTGTGTGTGTGTGTGTGTGTGTGTCATTATTACTCACGGTACGA
GT15mir182	GTGTGTGTGTGTGTGTGTGTGTGTGTGTGTGTGTTGTGAGTTCTACCATTGCCAAA
GT15mir152	GTGTGTGTGTGTGTGTGTGTGTGTGTGTGTGTGCCAAGTTCTGTGCATGCACTGA
GT15mir509	GTGTGTGTGTGTGTGTGTGTGTGTGTGTGTGTGTTGATTGCCACTGTCTGCAGTA
GT15mir96	GTGTGTGTGTGTGTGTGTGTGTGTGTGTGTGTAGCAAAAATGTGCTAGTGCCAAA
GT15mir183	GTGTGTGTGTGTGTGTGTGTGTGTGTGTGTGTAGTGAATTCTACCAGTGCCATA
GT15mir494	GTGTGTGTGTGTGTGTGTGTGTGTGTGTGTGTGAGGTTTCCCGTGTATGTTTCA
GT15mir39	GTGTGTGTGTGTGTGTGTGTGTGTGTGTGTGTCAAGCTGATTTACACCCGGTGA
GT15mir21	GTGTGTGTGTGTGTGTGTGTGTGTGTGTGTGTTCAACATCAGTCTGATAAGCTA
GT15mir141	GTGTGTGTGTGTGTGTGTGTGTGTGTGTGTGTCCATCTTTACCAGACAGTGTTA
GT15mir429	GTGTGTGTGTGTGTGTGTGTGTGTGTGTGTGTACGGTTTTACCAGACAGTATTA
GT15mir200b	GTGTGTGTGTGTGTGTGTGTGTGTGTGTGTGTTTCATCATTACCAGGCAGTATTA
GT15mir19-minus6	GTGTGTGTGTGTGTGTGTGTGTGTGTGTGTGTTTCAGTTTTGCATAGATT
GT6mir19-Cy5	GTGTGTGTGTGTTCAGTTTTGCATAGATTTGCACA - Cy5

Table S2. GT15mirX sequences used in this work.

Name	Sequence
GT15mir19	5' - GTGTGTGTGTGTGTGTGTGTGTGTGTGTGTGTGTTTCAGTTTTGCATAGATTTGCACA - 3'
mir19-10	3' - CTAAACGTGT - 5'
mir19-11	3' - TCTAAACGTGT - 5'
mir19-12	3' - ATCTAAACGTGT - 5'
mir19-13	3' - TATCTAAACGTGT - 5'
mir19-14	3' - GTATCTAAACGTGT - 5'
mir19-15	3' - CGTATCTAAACGTGT - 5'
mir19-17	3' - AACGTATCTAAACGTGT - 5'

Table S5. Truncated miR analyte sequences designed to hybridize to the 5' end of miRNA capture sequence.

Name	Sequence (5' to 3')
R23mir19R23	TCGGTCAGTGGGTCATTGCTAGTGTGCAAATCTATGCAAAACTGATCGGTCAGTGGGTCATTGCTAGT
mir19R23	TCGGTCAGTGGGTCATTGCTAGTGTGCAAATCTATGCAAAACTGA
R23mir19	TGTGCAAATCTATGCAAAACTGATCGGTCAGTGGGTCATTGCTAGT
R23R23R23	TCGGTCAGTGGGTCATTGCTAGTTCGGTCAGTGGGTCATTGCTAGTTCGGTCAGTGGGTCATTGCTAGT

Table S6. Elongated analyte sequences used in this work.

References

1. Jung, S., Cha, M., Park, J. et al. Dissociation of single-strand DNA: single-walled carbon nanotube hybrids by Watson-Crick base-pairing. *Journal of the American Chemical Society* **132**, 10964-10966 (2010).
2. Miyauchi, Y., Saito, R., Sato, K. et al. Dependence of exciton transition energy of single-walled carbon nanotubes on surrounding dielectric materials. *Chemical Physics Letters* **442**, 394-399 (2007).
3. Hagenmueller, R., Rahatekar, S.S., Fagan, J.A. et al. Comparison of the quality of aqueous dispersions of single wall carbon nanotubes using surfactants and biomolecules. *Langmuir : the ACS journal of surfaces and colloids* **24**, 5070-5078 (2008).
4. Fantini, C., Cassimiro, J., Peressinotto, V.S.T. et al. Investigation of the light emission efficiency of single-wall carbon nanotubes wrapped with different surfactants. *Chemical Physics Letters* **473**, 96-101 (2009).
5. Ohno, Y., Iwasaki, S., Murakami, Y. et al. Chirality-dependent environmental effects in photoluminescence of single-walled carbon nanotubes. *Physical Review B* **73** (2006).
6. Lesnik, E.A. & Freier, S.M. Relative Thermodynamic Stability of DNA, Rna, and DNA-Rna Hybrid Duplexes - Relationship with Base Composition and Structure. *Biochemistry* **34**, 10807-10815 (1995).
7. Gyi, J.I., Lane, A.N., Conn, G.L. & Brown, T. The orientation and dynamics of the C2'-OH and hydration of RNA and DNA-RNA hybrids. *Nucleic acids research* **26**, 3104-3110 (1998).